Available online at www.sciencedirect.com
ScienceDirect
Comput. Methods Appl. Mech. Engrg. 360 (2020) 112696
Computer methods in applied mechanics and engineering
www.elsevier.com/locate/cma

A hierarchical spline based isogeometric topology optimization using moving morphable components

Xianda Xie[a], Shuting Wang[a], Manman Xu[a], Ning Jiang[a], Yingjun Wang[b,*]

[a] School of Mechanical Science and Engineering, Huazhong University of Science and Technology, Wuhan, 430074, China
[b] National Engineering Research Center of Novel Equipment for Polymer Processing, Key Laboratory of Polymer Processing Engineering, Ministry of Education, Guangdong Provincial Key Laboratory of Technique and Equipment for Macromolecular Advanced Manufacturing, South China University of Technology, Guangzhou, 510641, China

Received 6 April 2019; received in revised form 10 October 2019; accepted 10 October 2019
Available online 22 October 2019

Abstract

This paper presents a hierarchical spline based isogeometric topology optimization using moving morphable components (HITO-MMC). In this work, the adaptive isogeometric analysis implemented by hierarchical B-spline is adopted to efficiently and accurately assess the structural performance. An ersatz material model is derived from the Gaussian points of the hierarchy computational mesh to relate the geometric design variables with the objective and constraint of TO. To determine the iterative steps performing local refinement and the elements to be locally refined, a mark strategy is put forward based on the relative error of objective function and the value of topological description function (TDF). The mathematic model of HITO-MMC is reformulated by mapping the global displacement vector into the local displacement vector of the active elements on each level of the hierarchy computational mesh. The proposed HITO-MMC approach has twofold merits: (a) the optimization can be started from a relative coarse computational mesh and the mesh is locally refined during the course of TO, which result into a highly computational efficiency; (b) more accurate results are obtained due to the use of high continuous hierarchical basis functions and denser mesh on structural boundary. Besides, continuous refinement is more effective to generate the optimal design than fixed NURBS mesh, and hierarchical local refinement is superior to continuous global refinement. The effectiveness of the proposed HITO-MMC is validated by a series of 2D and 3D numerical benchmarks.

Keywords: Topology optimization; IGA; Moving morphable components; Hierarchical local refinement

1. Introduction

Since the pioneering work of Bendsøe and Kikuchi [1], topology optimization (TO) has been fully developed over past three decades, and a series of TO methods have been proposed, e.g., solid isotropic material with penalization (SIMP) model [2], evolutionary approach [3], level set method [4–7], moving morphable components or voids (MMCs or MMVs) approach [8–11]. Due to its effectiveness in obtaining the optimal structure under some certain constraints within a specified design domain, TO has been successfully applied to a variety of

* Corresponding author.
E-mail address: wangyj84@scut.edu.cn (Y. Wang).

https://doi.org/10.1016/j.cma.2019.112696

engineering problems [12–17]. By integrating with Giga-voxel computational morphogenesis, the structure of a full-scale aeroplane wing is optimized by SIMP method elaborated in Nature [18]. The thermal conduction performance of a conductive heat transfer is improved by TO in [19]. To ensure the optimized structure by TO complying with the geometrical restrictions of additive manufacturing (AM), 3D structures which are fully self-supporting optimized designs are shown in [20].

Traditional finite element analysis (FEA) is used to obtain the unknown physical field during the optimization process of all aforementioned TO methods, which leads to numerical instabilities and checkerboard pattern [21] as well as the disconnection between analysis and geometric models [22]. These limitations can be successfully resolved by isogeometric analysis (IGA) firstly proposed by Hughes et al. in 2005 [23], which takes an exact geometric model in the analysis. Compared to traditional FEA, IGA has a higher continuity as well as a higher computational efficiency for high order elements. Therefore, IGA has been introduced into TO by scientific researchers in the last decade [24–26]. The high-continuous spline of IGA can circumvent the checkerboards appeared in TO without additional filters [27–29]. By integrating IGA with parameterized level set method, Wang et al. [30] proposed an more accurate and efficient isogeometric topology optimization (ITO) and then to satisfy some geometric restrictions, an arbitrary geometric constraint is added into such ITO models in [31]. Besides, an ITO scheme is constructed for the design of lattice materials based on the theory of asymptotic homogenization [32].

Due to the use of density or level set representation of the structure, the number of design variables is of the same order as the finite elements and there is no explicit structural boundary representation in the above mentioned ITO schemes. The drawbacks of huge design variables and lacking explicit geometric structural representation in these ITO schemes, can be addressed by the MMC-based TO [33]. By integrating the merits of IGA and MMC-based TO, an ITO-MMC scheme is proposed by Xie et al. [34] based on R-functions. The computational domain is discretized into relatively fine NURBS mesh to carry out the calculation of IGA in ITO-MMC, which brought heavy computational burden. According to the result shown in [35–37] where adaptive mesh refinement strategy is used, compared to global refinement, the local refinement of FEA can reduce the computational scale of FEA without weakening the structural performance of the optimal result, which results in the reduction of the number of degree of freedoms (DOFs). Similarly, the computational burden of the ITO-MMC method for optimizing TO problems can be decreased by discretizing the design domain with a relatively coarse mesh and performing the local refinement during the process of TO for the computational NURBS mesh.

In IGA, a fundamental topic is adaptivity, since the tensor product structure underlying the shape function of IGA (B-splines or NURBS) precludes local refinement and forces a global refinement. To overcome the aforementioned restriction, a series of local refinement techniques of IGA are emerging, e.g., T-Splines [38–40], LR-Splines [41], hierarchical B-Splines [42–45], hierarchical box splines [46]. Hierarchical B-Splines are constructed from the basis functions of nested approximation spaces with different hierarchical levels. Due to the linear independence of the basis and the rigorous proof of the linear independence, hierarchical B-spline is one of the most promising ways to equip IGA with local refinement [47]. The fundamental properties such as linear independence and partition of unity are assured by the theoretical properties of the spline space, and the hierarchical spline spaces have been integrated into isogeometric setting by Vuong et al. [43]. Then, Bornemann et al. proposed a subdivision projection technique and introduced it into relating the hierarchical B-splines on different levels [48]. Moreover, truncated hierarchical B-splines is an improved hierarchical B-splines where the partition-of-unity property is recovered and the interactions between basis functions on different hierarchical levels are alleviated [49–51].

In this paper, we take advantage of both MMC-based TO and the local refinement of IGA implemented by hierarchical B-splines, and firstly propose a framework of IGA with hierarchical spline based topology optimization using MMC (HITO-MMC). To locate the refined region of computational domain and determine the iterative steps performing the hierarchical local refinement along with the process of optimization, a geometrical mark strategy is presented, where the elements close to the boundary of the optimized structure are marked and chosen to be refined similar to those techniques used in [35,52–54], and the hierarchical local refinement will be triggered if the relative error of the value of the objective function is smaller than an upper limit. Different from the ersatz material model based on elemental nodes in [33], a new ersatz material model based on Gaussian quadrature points is introduced to conduct the sensitivity analysis of the non-uniform grid structure of the hierarchical mesh which has hanging elemental nodes. Besides, the sensitivity analysis based on IGA using hierarchical splines is constructed by exploiting the subdivision projection technique [48] and calculated level by level as a hierarchical structure.

The layout of this paper is described as follows. Section 2 presents the general construction of B-splines and adaptively refined hierarchical spline spaces. Afterwards, the MMC-based optimization model is reviewed, then the

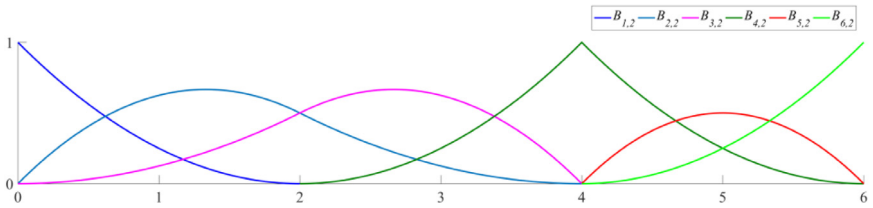

Fig. 1. Quadratic B-spline basis functions with interpolatory ends for an open knot vector $\boldsymbol{\Xi} = \{0, 0, 0, 2, 4, 4, 6, 6, 6\}$ are presented and the continuity of $B_{4,2}$ is C^0 observed from the curves since the multiplicity is 2 for the fifth knot of $\boldsymbol{\Xi}$.

model of HITO-MMC is proposed and elaborated in detail in Section 3. The numerical implementation of HITO-MMC is described in Section 4. Benchmark examples which verify the effectiveness of the established HITO-MMC are given in Section 5. Finally, the conclusions are drawn in Section 6.

2. Hierarchical refinement based on B-spline subdivision

In this section, we firstly review some basic definition of B-splines and NURBS, which are the key ingredients for IGA. Then, the technique aspects of the hierarchical local refinement for B-splines and NURBS are particularly emphasized. A comprehensive review can be obtained in [23,42,43,55,56], where a state of art of IGA and the hierarchical local refinement of IGA are provided for readers.

2.1. Definition of B-splines and NURBS basis function

The B-spline basis functions of degree p are formed from a sequence of non-decreasing knots referred to as a knot vector $\boldsymbol{\Xi} = \{\xi_1, \xi_2, \ldots, \xi_{n+p+1}\}$, which are commonly used to generate and represent the curves and surfaces in the system of computer aided design (CAD) and computer graphics (CG) [57]. With the definition of B-spline basis functions of degree $p = 0$ presented in Eq. (1), the B-spline basis functions of degree p ($p > 0$) are then constructed by the Cox–de Boor formula [58] formulated as Eq. (2).

$$B_{i,0} = \begin{cases} 1, & if \ \ \xi_i \le \xi < \xi_{i+p+1} \\ 0, & otherwise \end{cases}. \tag{1}$$

$$B_{i,p}(\xi) = \frac{\xi - \xi_i}{\xi_{i+p} - \xi_i} B_{i,p-1}(\xi) + \frac{\xi_{i+p+1} - \xi}{\xi_{i+p+1} - \xi_{i+1}} B_{i+1,p-1}(\xi). \tag{2}$$

The partition of unity $\sum_{i=1}^{n} B_{i,p}(\xi) = 1$ is one of the properties of B-spline basis functions. Besides, the smoothness of B-spline basis function is C^{p-k} at the location where a knot is repeated k times, and k is the multiplicity of the knot in $\boldsymbol{\Xi}$. The basis interpolatory will be guaranteed if $\boldsymbol{\Xi}$ is an open knot vector where the end knots have the multiplicity of $p + 1$. An example for the B-spline basis functions of an open knot vector $\boldsymbol{\Xi} = \{0, 0, 0, 2, 4, 4, 6, 6, 6\}$ is presented in Fig. 1.

On the basis of univariate B-splines, a univariate NURBS is formed from a projective transformation of a corresponding B-spline in $\mathbb{R}^2$ as:

$$R_{i,p}(\xi) = \frac{w_i B_{i,p}(\xi)}{\sum_{j=1}^{n} w_j B_{j,p}(\xi)}, \tag{3}$$

where $B_{i,p}(\xi)$ is the ith polynomial B-spline basis function and w_i is the corresponding weight.

The extensions of the univariate B-splines and NURBS to the multivariate case can be easily implemented by the tensor product. The multivariate basis functions $B_{\boldsymbol{i},\boldsymbol{p}}(\xi)$ are generated from the univariate B-spline basis functions B_{i_m,p_m} along the mth parametric direction as follows:

$$B_{\boldsymbol{i},\boldsymbol{p}}(\boldsymbol{\xi}) = \prod_{m=1}^{d_p} B_{i_m,p_m}(\xi_{i_m}^m), \tag{4}$$

where d_p denotes the dimension of the parameter space, $\boldsymbol{\Xi}^m = \left\{\xi_1^m, \xi_2^m, \ldots, \xi_{n_m+p_m+1}^m\right\}$ $(m = 1, \ldots, d_p)$ are the d_p univariate knot vectors, p_m is the polynomial degree along the parametric direction m, and n_m indicates the associated number of functions. On the left hand side of Eq. (4), $\boldsymbol{i} = (i_1, i_2, \ldots, i_{d_p})$ represents the index position in the tensor product structure, $\boldsymbol{p} = (p_1, p_2, \ldots, p_{d_p})$ indicates the polynomial degrees for all parameter directions, and $\boldsymbol{\xi} = (\xi_{i_1}^1, \xi_{i_2}^2, \ldots, \xi_{i_{d_p}}^{d_p})$ denotes the parametric coordinate.

Similarly, the multivariate NURBS are constructed as:

$$R_{\boldsymbol{i},\boldsymbol{p}}(\boldsymbol{\xi}) = \frac{w_{\boldsymbol{i}} B_{\boldsymbol{i},\boldsymbol{p}}(\boldsymbol{\xi})}{\sum_{\boldsymbol{j}} w_{\boldsymbol{j}} B_{\boldsymbol{j},\boldsymbol{p}}(\boldsymbol{\xi})}. \tag{5}$$

2.2. Subdivision refinement of univariate and multivariate B-splines

As pointed by Schillinger [45], subdivision is a remarkable property of uniform B-splines and the refinement is naturally implemented by subdivision. Due to the subdivision property, a two-scale relation can be presented as Eq. (6) [59–61] for a univariate B-spline basis function B_p of polynomial degree p.

$$B_p(\xi) = 2^{-p} \sum_{j=0}^{p+1} \binom{p+1}{j} B_p(2\xi - j). \tag{6}$$

The binomial coefficient used in Eq. (6) is formulated as:

$$\binom{p+1}{j} = \frac{(p+1)!}{j!\,(p+1-j)!}. \tag{7}$$

The original equidistantly spaced knot vector $\boldsymbol{\Xi}^0 = \{0, 1, 2, 3, \ldots\}$ is the knot vector on level 0, and the knot sequence $\boldsymbol{\Xi}^l = \left\{0, 1/2^l, 2/2^l, 3/2^l, \ldots\right\}$ is the knot vector on level l which is l-times bisected from $\boldsymbol{\Xi}^0$. By means of the two-scale relation as Eq. (6), a B-spline basis function $B_i^{l,p}$ on level l ($l \geq 0$) can be expressed as a linear combination of $B_j^{l+1,p}$ with the number of p+2 which are the children of $B_i^{l,p}$, and $B_i^{l,p}$ is referred to as the parent of $B_j^{l+1,p}$ inversely. The relation of B-splines on consecutive levels is defined as:

$$B_{i,p}^l(\xi) = \sum_k C_{i,k}^p B_{2i+k}^{l+1,p}(\xi) \quad \text{with } C_{i,k}^p = \frac{1}{2^p}\binom{p+1}{k} = \frac{1}{2^p}\frac{(p+1)!}{k!\,(p+1-k)!}, \tag{8}$$

where $C_{i,k}^p$ are the entities of the subdivision matrix which is a banded sparse matrix due to the local support of B-spline basis. Then, Eq. (8) can be rewritten in the matrix form for the sake of simplicity:

$$\boldsymbol{B}^{l,p} = \boldsymbol{C}^p \boldsymbol{B}^{l+1,p}. \tag{9}$$

With the help of the tensor product structure presented in Eq. (4), the extension of subdivision refinement of univariate B-splines is straightforward and formulated as:

$$B_{\boldsymbol{i}}^{l,p}(\boldsymbol{\xi}) = \boldsymbol{S}^p B_{\boldsymbol{i}}^{l+1,p}(\boldsymbol{\xi}) \quad \text{with } \boldsymbol{S}^p = S_{\boldsymbol{i},\boldsymbol{k}}^p = S_{\left(i_1,\ldots,i_{d_p}\right),\left(k_1,\ldots,k_{d_p}\right)}^p = \prod_{j=1}^{d_p} S_{i_j,k_j}^p. \tag{10}$$

For the B-spline basis functions defined by an open knot vector, the aforementioned two-scale relation presented in Eq. (6) do not hold any more, and it need to be generalized as:

$$B = \sum_i \varphi_i s_i, \tag{11}$$

where the original B-spline function B is expressed by several new B-spline functions φ_i and the corresponding scaling factors are represented by s_i. Moreover, the construction of corresponding knot vector and scaling factors are easily implemented by using the standard knot refinement algorithms [62,63].

2.3. Hierarchical local refinement from element viewpoint

In the context of hierarchical local refinement of IGA, both refinement triggered from element-wise and basis-wise strategies are adopted [45], and hierarchical local refinement from element viewpoint is used in this paper,

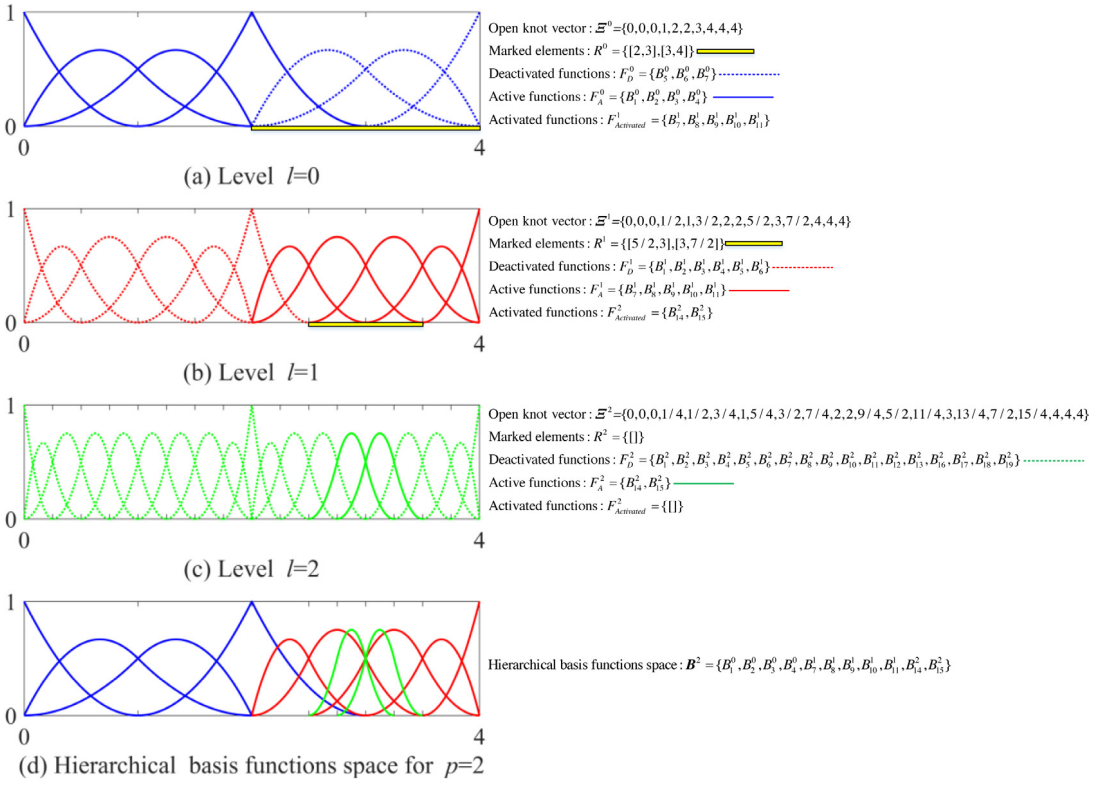

Fig. 2. The major aspects are demonstrated for constructing a hierarchical basis functions space by hierarchical local refinement algorithm.

since the proposed geometrical mark strategy for hierarchical local refinement is derived from quadrature points of each active element and adopting the element based local refinement offers the intuitive convenience.

The algorithm for creating a hierarchical basis function space is demonstrated for element-wise strategy and the key ingredients of hierarchical local refinement technique can be summarized as follows:

- Step 1 (Initial configuration): All basis functions at the coarsest level are activated initially and the level l is set to 0, as well as the sequences of open knot vector sequences are obtained by the h-refinement technique [23];
- Step 2 (Mark the elements): Mark the elements on level l in terms of the mark strategy and obtain the set of marked elements R^l;
- Step 3 (Functions deactivation): Deactivate the basis B_i^l whose support supp B_i^l belongs to R^l;
- Step 4: (Function Activation): Activate the basis B_i^{l+1} whose support supp B_i^{l+1} is a subset of R^l;
- Step 5 (Loop operation): Set $l = l + 1$ and perform the steps from 2 to 5 until the max hierarchical level $N_0 - 1$ is reached.

An example for univariate B-splines is depicted in Fig. 2, with a schematic description of the aforementioned key ingredients of hierarchical local refinement technique.

Due to the tensor product structure of multivariate B-splines, the hierarchical local refinement strategy for multivariate B-splines can be easily implemented by performing the hierarchical local refinement strategy for each component of multivariate B-splines. Here, an example of a square shaped domain illustrated in Fig. 3 is used to demonstrate the hierarchical local refinement method for the multivariate case.

3. Hierarchical IGA based topology optimization using MMC

Beginning with a brief review of TO using MMC method, a novel mathematic model of TO using MMC is subsequently put forward, which integrates the technique of hierarchical local refinement for IGA. Moreover, to obtain the iterative steps carrying out the hierarchical local refinement and the refined regions during the process of optimization, a mark strategy is presented in this section as well. To avoid difficulties with the notation, the TO

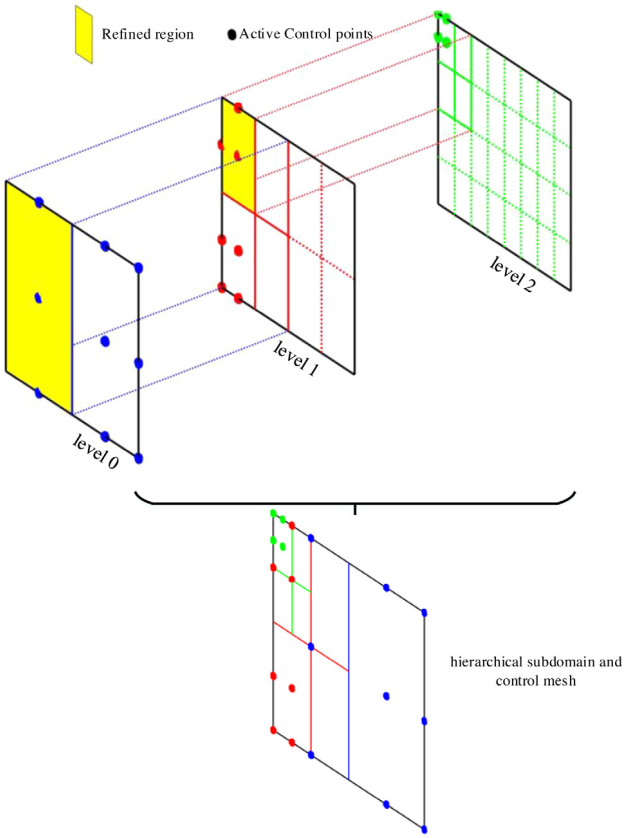

Fig. 3. The hierarchical local refinement strategy for bivariate case is demonstrated with NURBS elements of which the degree is 2 for each parameter direction. The active functions are indicated by the corresponding active control points. Four elements of level 2, three elements of level 1 and one element of level 0 constitute the final hierarchical subdomain set, which are referred to as active elements.

problem for compliance minimization is only considered, which can be generalized to other types of TO problems with limited efforts of modification.

3.1. Topology optimization using MMC

According to the definition in the work of Guo et al. [33,64], the mathematic model of TO for compliance minimization using MMC is formulated as follows:

$$\begin{aligned} &Find\ \boldsymbol{D} = (\boldsymbol{D}_1^{\mathrm{T}}, \boldsymbol{D}_2^{\mathrm{T}}, \ldots, \boldsymbol{D}_n^{\mathrm{T}})^{\mathrm{T}} \\ &Minimize\, C = \boldsymbol{F}^{\mathrm{T}}\boldsymbol{u} \\ &s.t. \\ &\boldsymbol{K}\boldsymbol{u} = \boldsymbol{F} \\ &g_v(\boldsymbol{D}) \le 0 \\ &\boldsymbol{D} \subset \mathcal{U}_{\boldsymbol{D}} \end{aligned}, \tag{12}$$

where C denotes the objective function, $\boldsymbol{F}$ is the external force vector, $\boldsymbol{u}$ is the displacement vector, $g_v(\boldsymbol{D})$ represents the volume constraint function, the set of design variables $\boldsymbol{D}$ consists of all geometric design variables with the subset represented by $\boldsymbol{D}_i^{\mathrm{T}} = (x_{0i}, y_{0i}, L_i, t_{1i}, t_{2i}, t_{3i}, \theta_i)$, which corresponds to a component possessing a similar configuration as depicted in Fig. 4 and consists of the component central coordinates (x_{0i}, y_{0i}), half-length (L_i) along the direction x′, inclined angle (θ_i) between global and local coordinate system, and variable depth $\boldsymbol{t}_i = (t_{1i}, t_{2i}, t_{3i})$. In Eq. (12), $\mathcal{U}_{\boldsymbol{D}}$ is the admissible set of $\boldsymbol{D}$ and n is the number of components constituting the topology of the structure.

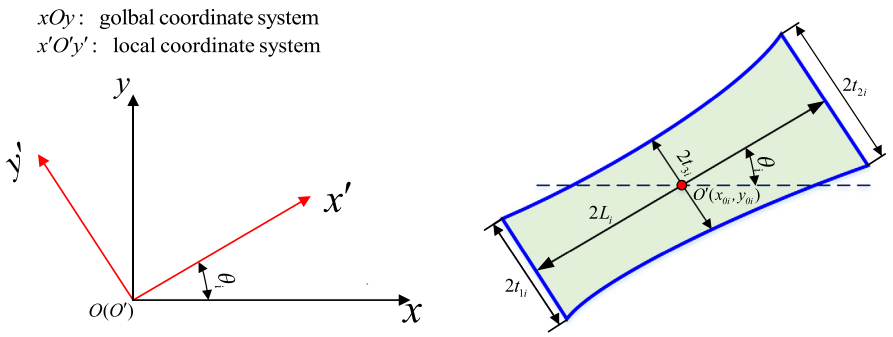

Fig. 4. The geometry and coordinate system for a component used in TO using MMC method.

In a design domain D with solid region Ω^s, the structural topology can be implicitly expressed by:

$$\begin{cases} \varphi^s(x) > 0, & if\ x \in \Omega^s \\ \varphi^s(x) = 0, & if\ x \in \partial\Omega^s \\ \varphi^s(x) < 0, & if\ x \in D \backslash \Omega^s \end{cases}, \tag{13}$$

where

$$\varphi^s(x) = max(\varphi_1, \ldots, \varphi_n). \tag{14}$$

In Eq. (14), φ_i with $i = 1, 2, \ldots, n$ means the TDF of the ith component, which is written as:

$$\varphi_i(x, y) = \left(\frac{x'}{L_i}\right)^p + \left(\frac{y'}{f(x')}\right)^p - 1\ (p = 6)\,, \tag{15}$$

with

$$\begin{Bmatrix} x' \\ y' \end{Bmatrix} = \begin{bmatrix} \cos\theta_i & \sin\theta_i \\ -\sin\theta_i & \cos\theta_i \end{bmatrix} \begin{Bmatrix} x - x_{0i} \\ y - y_{0i} \end{Bmatrix}, \tag{16}$$

and

$$f(x') = \frac{t_{1i} + t_{2i} - 2t_{3i}}{2L_i^2}(x')^2 + \frac{t_{2i} - t_{1i}}{2L_i}x' + t_{3i}. \tag{17}$$

3.2. Mathematic model of TO using IGA with hierarchical splines

The ersatz material model is one of the key ingredients of TO, which acts as a bridge between the design variables and objectives (or constraints) of the optimization problem. Sound ersatz material model is of significance to the convergence and stability of optimization process. Therefore, an appropriate ersatz material model should be taken into consideration before the presentation of mathematic model of TO using hierarchical IGA. In this work, the ersatz material model is established based on the values of TDF of Gaussian points, which is different from those used in traditional FEM based MMC method [65] or ITO-MMC [34]. The reasons to not use the ersatz material model in the two contributions mentioned above are as follows: the strain energy of the nodes of an active element cannot be calculated by the sum of one fourth of the strain energy of elements surrounding to the corresponding point, due to the existence of the hanging nodes in the hierarchical mesh (see Fig. 5(a)); the strain energy of multi-level Greville abscissae is difficult to compute, since those points are not properly graded in the overlap of the supports of functions with different levels [66] and the strain energy of active elements on the finer level may contribute to the strain energy of Greville abscissae of active elements on the coarser level (see Fig. 5(b)). Therefore, these two schemes will lead to inaccurate sensitivity analysis resulted from the inaccurate nodal or Greville abscissae strain energy, which will deteriorate the convergence of TO. The Gaussian points of a hierarchical NURBS mesh are accurate to the sensitivity analysis of TO, since Gaussian points located in the interior of active elements are

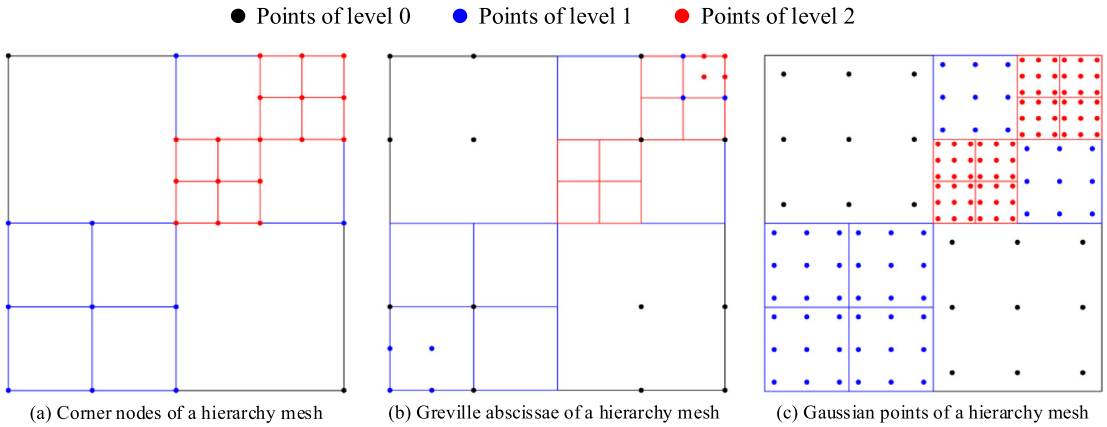

Fig. 5. An illustration for the positions of multi-level corner nodes, Greville abscissae and Gaussian points of a hierarchy mesh with three different mesh sizes.

not encircled by elements with different mesh sizes and properly graded in each active element (see Fig. 5(c)), and the feature of spanning over several active elements on different levels is disappeared for Gaussian points. Hence, the ersatz material model used in this paper is based on Gaussian points of all active elements of the hierarchy computational mesh.

With the use of Gaussian points obtained from Gaussian quadrature, the ersatz material model for TO using hierarchical IGA is constructed as follows. Firstly, TDF values of Gaussian points are calculated by Eq. (14). Then, the regularized Heaviside function formulated as Eq. (18) is introduced to transform the TDF values of Gaussian points into regularized Heaviside values, which spread over the range of [0, 1]. Finally, the new ersatz material model is established based on the regularized Heaviside values of the corresponding Gaussian points for each active element and written in the form of Eq. (19).

$$H_\varepsilon(x) = \begin{cases} 1 & if\ x > \varepsilon \\ \dfrac{3(1-\beta)}{4}\left(\dfrac{x}{\varepsilon} - \dfrac{x^3}{3\varepsilon^3}\right) + \dfrac{1+\beta}{2} & if\ -\varepsilon \le x \le \varepsilon\ , \\ \beta & if\ x < -\varepsilon \end{cases} \tag{18}$$

where β denotes a small positive constant to ensure the nonsingularity of global stiffness matrix and ε represents a constant parameter to control the level of regularization.

$$\begin{cases} \gamma_e^l = \dfrac{1}{n_{gp}}\left(\displaystyle\sum_{i=1}^{n_{gp}} H_\varepsilon^q(\varphi_{i,e}^l)\right) \\ \rho_e^l = \dfrac{1}{n_{gp}}\left(\displaystyle\sum_{i=1}^{n_{gp}} H_\varepsilon(\varphi_{i,e}^l)\right) \end{cases} \quad e = 1, 2, \ldots, N_e^l \ \ and\ \ l = 0, 1 \cdots, N_0 - 1. \tag{19}$$

In Eq. (19), γ_e^l and ρ_e^l represent the Young's modulus coefficient and density of the eth active element on level l respectively, n_{gp} is the number of Gaussian points of an active element, $\varphi_{i,e}^l$ denotes the TDF value of the ith Gaussian point of the eth active element on level l, $H_\varepsilon(\varphi_{i,e}^l)$ expresses the corresponding regularized Heaviside value, N_e^l is the number of active elements on level l, $N_0 - 1$ represents the max hierarchical level of the hierarchy mesh, and q is set to 2 in this paper as those used in [8,34,64].

After obtaining the established ersatz material model, the formula shown in Eq. (12) for TO using MMC can be reformulated by adding the corresponding assumptions of mechanical model and specifying a volume constraint (see Eq. (8) of [64]). Therefore, the mathematic model of the proposed IGA with hierarchical splines based TO

using MMC (HITO-MMC) model is formulated as follows:

$$\begin{aligned}
&Find\ \boldsymbol{D} = (\boldsymbol{D}_1^{\mathrm{T}}, \boldsymbol{D}_2^{\mathrm{T}}, \ldots, \boldsymbol{D}_n^{\mathrm{T}})^{\mathrm{T}}, \boldsymbol{u}(\boldsymbol{x}) \\
&Minimize\ C = \sum_{l=0}^{N_0-1} \sum_{e=1}^{N_e^l} \gamma_e^l (\boldsymbol{u}_e^l)^{\mathrm{T}} \boldsymbol{K}_e^l \boldsymbol{u}_e^l \\
&s.t. \\
&\boldsymbol{K} \bullet \boldsymbol{u} = \boldsymbol{F} \\
&with\ \boldsymbol{K} = \left(\sum_{l=0}^{N_0-1} (\boldsymbol{C}^l)^{\mathrm{T}} \boldsymbol{K}^l \boldsymbol{C}^l \right) \quad where\ \boldsymbol{K}^l = \sum_{e=1}^{N_e^l} \gamma_e^l \boldsymbol{K}_e^l \\
&\sum_{l=0}^{N_0-1} \sum_{e=1}^{N_e^l} \rho_e^l V_e^l \le \overline{V}, \\
&\boldsymbol{D} \subset \mathcal{U}_{\boldsymbol{D}}
\end{aligned} \tag{20}$$

where $\boldsymbol{D}$ is the set of design variables consisting of geometric parameters of all components, C represents the structural mean compliance, $\boldsymbol{u}_e^l$ denotes the displacement vector of the control points associated with the eth active element on level l, $\boldsymbol{u}$ represents the displacement vector of all active control points, $\boldsymbol{K}$ is the global stiffness matrix of the control points corresponding to the linearly independent hierarchical basis functions space $\boldsymbol{B}^{N_0-1}$ as illustrated in Fig. 2, $\boldsymbol{K}_e^l$ is the stiffness matrix of the eth active NURBS element on level l with the density equaling to 1, $\boldsymbol{C}^l$ represents a transformation matrix to transform the stiffness matrix of all active elements on level l into the global stiffness matrix $\boldsymbol{K}$, V_e^l denotes the volume of the eth active element on level l, $\overline{V}$ is the prescribed volume fraction, $\mathcal{U}_{\boldsymbol{D}}$ represents the admissible set where $\boldsymbol{D}$ belongs.

3.3. Mark strategy for hierarchical local refinement

One of the key ingredients for the proposed HITO-MMC framework is the mark strategy of hierarchical local refinement, which can change the hierarchy mesh adaptively along with the process of TO. The mark strategy consists of two parts: a criterion g_{step} used to trigger the hierarchical local refinement or not, and a geometric mark criterion g_M for detecting the elements to be marked and locally refined.

To determine the iterative steps where the hierarchical local refinement should be proceeded for the associated hierarchy computational mesh, the criterion presented in Eq. (21) is put forward similar to the strategy used in [36], the tolerance of adaptive mesh refinement tol_{AMR} has an initial value and is updated by halving its value after each execution of a hierarchical local refinement.

$$\begin{aligned}
&g_{step} = \begin{cases} 1, & if\ \ \left| C_k - \overline{C}_k \right| / \overline{C}_k \le tol_{AMR} \\ 0, & otherwise \end{cases} \\
&with\ \overline{C}_k = \sum_{i=0}^{9} C_{k-i} \Big/ 10 \quad k \ge 10
\end{aligned}, \tag{21}$$

where C_k denotes the value of objective function at the kth iterative step, $\overline{C}_k$ represents the mean value of the last ten iterative steps counting backwards from the kth iterative step.

Similar to the strategy capturing the region to be refined in [35], a geometric mark criterion $g_{M,e}^l$ is proposed herein for detecting the active elements on level l in the vicinity of the structural boundary. With the use of the TDF values at Gaussian points calculated by Eq. (15), the geometric mark criterion $g_{M,e}^l$ is formulated as follows:

$$\begin{aligned}
&g_{M,e}^l = \begin{cases} 1 & \text{if } \exists -tol_{TDF}^l \le \varphi_{i,e}^l \le tol_{TDF}^l (i = 1, 2, \ldots, n_{gp}) \\ 0 & otherwise \end{cases} \quad e = 1, 2, \ldots, N_e^l \ \ and \ \ l = 0, 1, \ldots, N_0 - 1 \\
&with\ tol_{TDF}^l = tol_{TDF}^0 / l
\end{aligned}, \tag{22}$$

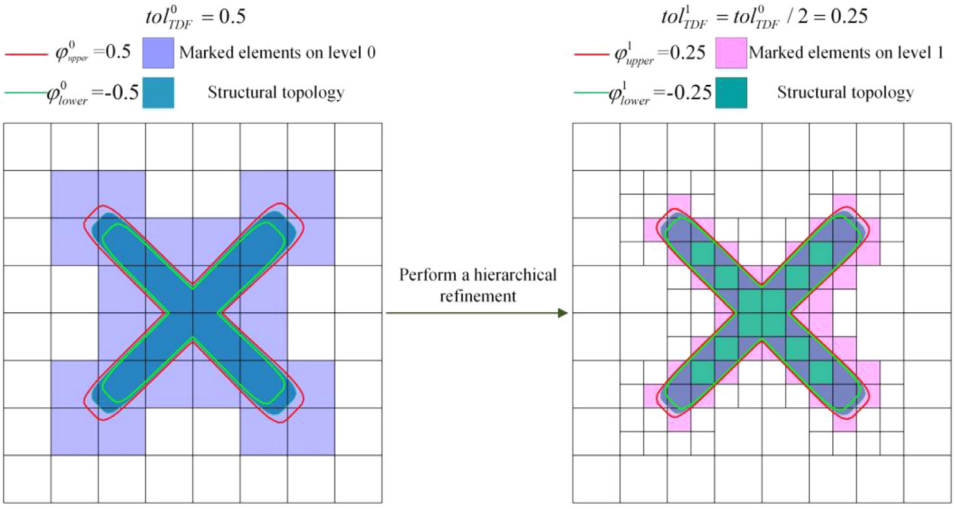

Fig. 6. The marked region for a uniform NURBS mesh with size of 8×8 is shown in the left, both the hierarchical mesh obtained from refining the marked region in purple and the corresponding pink marked elements for active elements on level 1 are shown in the right.

where tol^0_{TDF} is the initial value of the parameter used to define the region close to the structural boundary for the initial NURBS mesh, tol^l_{TDF} is the parameter to get the marked elements for the active elements on level l, which is obtained from dividing tol^0_{TDF} by l. An illustration for the geometric mark criteria $g^l_{M,e}$ proposed in this paper is depicted in Fig. 6.

4. Isogeometric analysis with hierarchical splines for HITO-MMC

For the minimum compliance problem, the equivalent integral equation can be written in Eq. (23) as a weak form.

$$\int_{\Omega_P} \varepsilon(\boldsymbol{v}) \cdot \mathbb{E} \cdot \varepsilon(\boldsymbol{u}) d\Omega_P = \int_{\Omega} \boldsymbol{v} \cdot \boldsymbol{f}\, d\Omega_P + \int_{\Gamma_t} \boldsymbol{v} \cdot \boldsymbol{t}\, d\Gamma_t \quad \forall \boldsymbol{v} \in \mathcal{U}_{ad}, \tag{23}$$

where Ω_P is the design domain, ε and $\mathbb{E}$ denote the second order linear strain tensor and the fourth order isotropic elasticity tensor of the solid material, respectively, $\boldsymbol{v}$ is an arbitrary test function within the admissible set $\mathcal{U}_{ad}$, $\boldsymbol{u}$ denotes the displacement field, $\boldsymbol{f}$ represents the body force, and $\boldsymbol{t}$ is the external force applied to the force boundary Γ_t.

According to the contents in Section 2, a linear independent hierarchical space is denoted by $\boldsymbol{B}^{N_0-1} = \cup_{l=0}^{N_0-1} F^l_A$. Using the isogeometric paradigm, both test function $\boldsymbol{v}$ and displacement field $\boldsymbol{u}$ are represented by the linear combination of basis functions of the given hierarchical space as follows:

$$\begin{aligned} &for\ \forall \boldsymbol{v}\ and\ \forall \boldsymbol{u}\,, \quad \exists \boldsymbol{q}_i\ and\ \exists \boldsymbol{u}_j \\ &s.t. \\ &\boldsymbol{v} = \sum_{i=1}^{n_{cp}} B_i \boldsymbol{q}_i, \qquad \boldsymbol{u} = \sum_{j=1}^{n_{cp}} B_j \boldsymbol{u}_j\,, \end{aligned} \tag{24}$$

where $\boldsymbol{q}_i$ and $\boldsymbol{u}_j$ are the vectors of constants, n_{cp} is the number of control points corresponding to the active basis functions in the hierarchical space $\boldsymbol{B}^{N_0-1}$. Due to the arbitrariness of $\boldsymbol{q}_i$, Eq. (23) can be rewritten as:

$$\sum_{j=1}^{n_{cp}} \int_{\Omega_P} \mathbf{B}_i^{\mathrm{T}} \mathbf{D} \mathbf{B}_j d\Omega_P \boldsymbol{u}_j = \int_{\Omega_P} B_i \boldsymbol{f} d\Omega_P + \int_{\Gamma_t} B_i \boldsymbol{t} d\Gamma_t, \tag{25}$$

where $\mathbf{D}$ is the stress–strain matrix, $\mathbf{B}_i$ represents a gradient matrix which is formulated as Eq. (26) for two dimensional case.

$$\mathbf{B}_i = \begin{bmatrix} \dfrac{\partial B_i}{\partial x} & 0 \\ 0 & \dfrac{\partial B_i}{\partial y} \\ \dfrac{\partial B_i}{\partial x} & \dfrac{\partial B_i}{\partial y} \end{bmatrix}. \tag{26}$$

Then, a matrix form of Eq. (25) is obtained and formulated as:

$$\begin{aligned} &\boldsymbol{K}\boldsymbol{u} = \boldsymbol{F} \\ &with\ \boldsymbol{K} = [\boldsymbol{K}_{ij}],\ \boldsymbol{K}_{ij} = \int_{\Omega_P} \boldsymbol{B}_i^{\mathrm{T}} \boldsymbol{D} \boldsymbol{B}_j d\Omega_P \\ &\qquad \boldsymbol{u} = \{\boldsymbol{u}_i\} \\ &\qquad \boldsymbol{F} = \{\boldsymbol{F}_i\},\ \boldsymbol{F}_i = \int_{\Omega_P} B_i \boldsymbol{f} d\Omega_P + \int_{\Gamma_{\boldsymbol{t}}} B_i \boldsymbol{t} d\Gamma_{\boldsymbol{t}} \\ &\qquad i, j = 1, 2, \ldots, n_{cp} \end{aligned}, \tag{27}$$

where $\boldsymbol{K}$ is the global stiffness matrix, $\boldsymbol{u}$ represents the displacement vector for all DOFs, $\boldsymbol{F}$ denotes the force vector.

Since the active functions on the coarser level may not vanish in active elements on the finer level as depicted in Fig. 3, the entities $\boldsymbol{K}_{ij}$ of $\boldsymbol{K}$ should be computed level by level as follows:

$$\boldsymbol{K}_{i,j} = \int_{\Omega_P} \mathbf{B}_i^{\mathrm{T}} \mathbf{D} \mathbf{B}_j d\Omega_P = \sum_{l=\max\{l_i, l_j\}}^{N_0-1} \left(\sum_{k=1}^{N^l} \sum_{k'=1}^{N^l} \left(\boldsymbol{c}_{ki}^{l_i,l} \right)^{\mathrm{T}} \int_{T^l} \mathbf{B}_k^{\mathrm{T}} \mathbf{D} \mathbf{B}_{k'} dT^l \boldsymbol{c}_{k'j}^{l_j,l} \right), \tag{28}$$

where l_i and l_j are the level of B_i and B_j respectively, T^l is the union of active elements on level l, N^l represents the number of control points corresponding to the active elements on level l, $\boldsymbol{c}_{ki}^{l_i,l}$ is a transformation matrix between $\mathbf{B}_i^{\mathrm{T}}$ and $\mathbf{B}_k^{\mathrm{T}}$, of which the component $c_{t_1,\ldots,t_{N_{DOF}}}^{l_i,l}$ is obtained based on the chain rule and the two-scale relation presented in Eq. (11) as:

$$\begin{aligned} &c_{t_1,\ldots,t_{N_{DOF}}}^{l_i,l} = \begin{cases} 1 & if\ l - l_i = 0 \\ \prod_{j=1}^{l-l_i} c_{t_1,\ldots,t_{N_{DOF}}}^{l_i+j-1,l_i+j} & if\ l - l_i \geq 1 \end{cases} \\ &with\ t_i = i,\ i + n_{cp} \cdots,\ i + (N_{DOF} - 1) \cdot n_{cp}\ and\ i = 1, \ldots,\ N_{DOF}, \end{aligned} \tag{29}$$

where N_{DOF} is the number of DOFs at each control point.

The coefficients used in Eq. (28) constitute a transformation matrix $\boldsymbol{C}_1$, which collects the coefficients for expressing the active hierarchical basis functions of DOFs up to level l by the basis functions corresponding to the DOFs of the active elements on level l. The size of the transformation matrix $\boldsymbol{C}_1$ is $N^l \cdot N_{DOF} \times N_A^{0:\,l} \cdot N_{DOF}$ where $N_A^{0:\,l}$ denotes the number of active functions up to level l. Therefore, Eq. (28) can be reformulated as:

$$\begin{aligned} \boldsymbol{K}_{i,j} &= \sum_{l=\max l_i, l_j}^{N_0-1} (\boldsymbol{C}_1)^{\mathrm{T}} \left(\sum_{k=1}^{N^l} \sum_{k'=1}^{N^l} \int_{T^l} \mathbf{B}_k^{\mathrm{T}} \boldsymbol{D} \mathbf{B}_{k'} dT^l \right) \boldsymbol{C}_1 = \sum_{l=\max l_i, l_j}^{N_0-1} (\boldsymbol{C}_1)^{\mathrm{T}} \sum_{e=1}^{N_e^l} \boldsymbol{K}_e^l \boldsymbol{C}_1 \\ &= \sum_{l=\max l_i, l_j}^{N_0-1} (\boldsymbol{C}_1)^{\mathrm{T}} \boldsymbol{K}^l \boldsymbol{C}_1 \\ &with\ \boldsymbol{K}^l = \sum_{e=1}^{N_e^l} \boldsymbol{K}_e^l\ and\ \boldsymbol{K}_e^l = \int_{T_e^l} \mathbf{B}^{\mathrm{T}} \mathbf{D} \mathbf{B} dT^l \end{aligned}. \tag{30}$$

Hence, the global stiffness matrix $\boldsymbol{K}$ is assembled by the submatrices $\boldsymbol{K}^l$ $\mathrm{l} = 0, \ldots, N_0 - 1$ as follows:

$$\boldsymbol{K} = \sum_{l=0}^{N_0-1} (\boldsymbol{C}^l)^{\mathrm{T}} \boldsymbol{K}^l \boldsymbol{C}^l \tag{31}$$

$$with\, \boldsymbol{C}^l = [\boldsymbol{C}_l\, \boldsymbol{0}]. \tag{32}$$

Similarly, the global force vector is assembled by the sub-vectors $\boldsymbol{F}^l$ with $\mathrm{l} = 0, \ldots, N_0 - 1$ and formulated as:

$$\boldsymbol{F} = \sum_{l=0}^{N_0-1} (\boldsymbol{C}^l)^{\mathrm{T}} \boldsymbol{F}^l \quad . \tag{33}$$

$$with\, \boldsymbol{C}^l = [\boldsymbol{C}_l\, \boldsymbol{0}]$$

In both Eqs. (32) and (33), $\boldsymbol{C}^l$ is the transformation matrix mapping the active functions of the hierarchical space $\boldsymbol{B}^{N_0-1}$ into the linear combination of the B-spline basis functions corresponding to the active elements on level l with size of $N^l \cdot N_{DOF} \times N_A^{0:\,\mathrm{N_0}-1} \cdot N_{DOF}$. Apparently, Eq. (23) is also fulfilled for the active elements on level l and results in:

$$\boldsymbol{K}^l \boldsymbol{u}^l = \boldsymbol{F}^l \quad for\ l = 0, 1, \ldots, N_0 - 1, \tag{34}$$

where $\boldsymbol{u}^l$ is the displacement vector for the control points associated with the active elements on level l.

Substituting Eqs. (32), (33) and (34) into Eq. (27), the relationship between the displacement vector $\boldsymbol{u}^l$ of level l and the displacement vector $\boldsymbol{u}$ of all active control points is formulated as:

$$\boldsymbol{u}^l = \boldsymbol{C}^{\mathrm{l}} \boldsymbol{u} \quad for\ l = 0, 1, \ldots, N_0 - 1, \tag{35}$$

which is critical to the sensitivity analysis for the proposed HITO-MMC.

Two dimensional (2D) plane stress problems are only taken into consideration in this part for the sake of simplicity, the strain–displacement matrix $\mathbf{B}$ and the stress–strain matrix $\mathbf{D}$ used in Eq. (30) are formulated as:

$$\mathbf{B} = \begin{bmatrix} \frac{\partial N_1}{\partial x} & 0 & \cdots & \frac{\partial N_{N^1}}{\partial x} & 0 \\ 0 & \frac{\partial N_1}{\partial y} & \cdots & 0 & \frac{\partial N_{N^1}}{\partial x} \\ \frac{\partial N_1}{\partial x} & \frac{\partial N_1}{\partial y} & \cdots & \frac{\partial N_{N^1}}{\partial x} & \frac{\partial N_{N^1}}{\partial y} \end{bmatrix}, \tag{36}$$

$$\mathbf{D} = \frac{E}{1-v^2} \begin{bmatrix} 1 & v & 0 \\ v & 1 & 0 \\ 0 & 0 & \frac{1-v}{2} \end{bmatrix}$$

where E and v denote the Young's modulus and Poisson's ratio, respectively.

With the ersatz material model defined in Eq. (19), the Young's modulus of the eth active element on level l is written as:

$$E_e^l = \gamma_e^l E \quad e = 1, 2, \ldots, N_e^l, \ l = 0, 1, \ldots, N_0 - 1. \tag{37}$$

Accordingly, the element stiffness of the eth active element on level l is interpreted as:

$$\overline{\boldsymbol{K}}_e^l = \int_{T_e^l} \mathbf{B}^{\mathrm{T}} \mathbf{D} \mathbf{B} \frac{E_e^l}{E} dT^l = \gamma_e^l \int_{T_e^l} \mathbf{B}^{\mathrm{T}} \mathbf{D} \mathbf{B} dT = \gamma_e^l \boldsymbol{K}_e^l, \tag{38}$$

where $\boldsymbol{K}_e^l$ represents the fully solid element stiffness matrix of the eth active element on level l.

Therefore, the proposed HITO-MMC presented in Eq. (20) can be reformulated as:

$$\begin{aligned} &Find\ \boldsymbol{D} = (\boldsymbol{D}_1^{\mathrm{T}}, \boldsymbol{D}_2^{\mathrm{T}}, \ldots, \boldsymbol{D}_n^{\mathrm{T}})^{\mathrm{T}}, \boldsymbol{u}(\boldsymbol{x}) \\ &Minimize\ C = \sum_{l=0}^{N_0-1} \sum_{e=1}^{N_e^l} (\boldsymbol{u}_e^l)^{\mathrm{T}} \overline{\boldsymbol{K}}_e^l \boldsymbol{u}_e^l \quad \left(\boldsymbol{u}_e^l = \boldsymbol{C}_e^l \boldsymbol{u} \quad for\ e = 0, 1, \ldots, N_e^l\right) \\ &s.t. \\ &\left(\sum_{l=0}^{N_0-1} (\boldsymbol{C}^l)^{\mathrm{T}} \sum_{e=1}^{N_e^l} \overline{\boldsymbol{K}}_e^l \boldsymbol{C}^l \right) \cdot \boldsymbol{u} = \boldsymbol{F} \\ &\sum_{l=0}^{N_0-1} \sum_{e=1}^{N_e^l} \rho_e^l V_e^l \le \overline{V}, \\ &\boldsymbol{D} \subset \mathcal{U}_{\boldsymbol{D}} \end{aligned} \quad , \tag{39}$$

where $\boldsymbol{C}_e^l$ is a submatrix of $\boldsymbol{C}^l$ associated with the eth active element on level l.

5. Computational examples

To verify the effectiveness of the proposed HITO-MMC, four benchmarks of minimization compliance problem are presented in this part. Due to the major concerns about the numerical performances, the material properties, geometry data of the design domain and external load applied to the structure are dimensionless. The Young's modulus E and Poisson's ratio v used in Eq. (36) are set to 1 and 0.3, respectively. As for the optimizer used in HITO-MMC, the Method of Moving Asymptotes (MMA) [67] is adopted, where the parameters are prescribed to epsimin = 10^(−10), raa0 = 0.01, albefa = 0.4, asyinit = 0.1, asyincr = 0.8, asydecr = 0.6. The operating environment for the examples is a workstation where the intel core is Xeon(R) Gold 5120 CPU @ 2.20 GHz 2.19 GHz, the RAM is 64 GB, the OS is Windows 10, and the software environment is MATLAB 2016a. For all examples, the max iterations are set to 300, and the max hierarchical level is prescribed to 10, as well as the initial value of the parameter tol_{AMR} used in Eq. (21) is fixed to 0.001 to obtain the iterative steps where the hierarchical local refinement should be conducted for the computational mesh with quadratic NURBS elements. The number of DOFs is expressed by a variable *dofs* in figures. Finally, the convergence criterion is set to $\theta_i = \left|C_i - \overline{C}_i\right| / \overline{C}_i \le 5 \times 10^{-5}$ with $\overline{C}_i = \sum_{j=0}^{9} C_{i-j}/10$ for $i = 10, 11, 12, \ldots$.

5.1. The Messerschmitt–Bolkow–Blohm (MBB) beam

In this benchmark, the well-known MBB beam is used to examine the effectiveness of the proposed HITO-MMC. Due to the symmetry of MBB beam, only half of MBB beam is taken into consideration. The design domain and boundary condition as well as the volume constraint for the half MBB beam are shown in Fig. 7, where the dimension of the design domain is 3 × 1, the load F is applied to the left-top corner with vertically downward direction, the upper bound of volume of solid material is specified to 0.4. The parameter tol_{TDF}^0 used in Eq. (22) is prescribed to 0.48 for the proposed mark strategy to determine the elements to be refined. Besides, the initial NURBS mesh with size of 45 × 15 is used to discretize the design domain. Both the initial uniform computational mesh and the initial design of basic structural components are illustrated in Fig. 8.

The hierarchy computational meshes, and the structural topologies, as well as the DOFs corresponding to the hierarchy computational meshes, are presented in Fig. 9 for the intermediate iterative steps with a local refinement performed. From the results shown in Fig. 9, it is noting that the mark strategy is effective to get the steps performing a local refinement and refine the region close to the structural boundary, the elements satisfying the mark condition presented in Eq. (22) are subdivided into four equal subelements. Some elements not on the boundary of any component are marked to be refined as shown in Fig. 9, which is resulted from the fact the geometric mark strategy is based on Gaussian quadrature points, of which the distribution is much denser than the nodal points of a fixed 90 × 30 grid used to display the structural components, and small components are only captured by the denser Gaussian quadrature points. Hence, the validity of the mark strategy proposed in this paper is verified for HITO-MMC. Afterwards, the final optimized structure and the corresponding hierarchical mesh as well as the convergence history are depicted in Fig. 10. Compared to the result of half MBB beam by ITO-MMC in [34], the number of

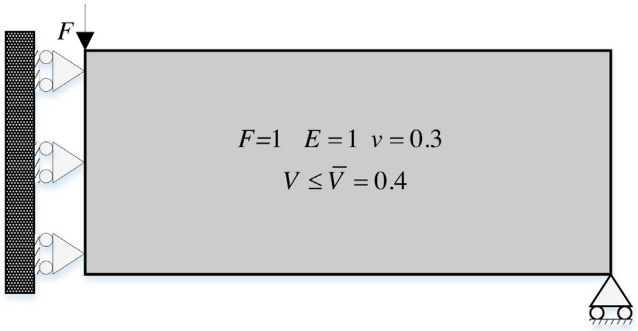

Fig. 7. The half MBB beam problem setting.

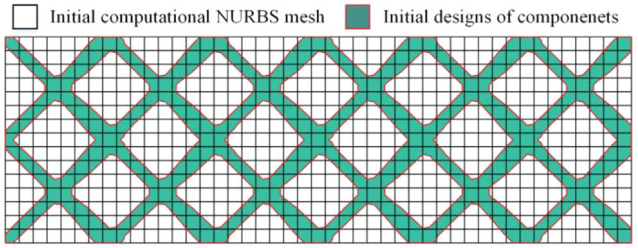

Fig. 8. The initial uniform computational mesh and the initial design for basic structural components.

iterations is reduced from 533 to 232 and the objective function is decreased from 229.94 to 204.48, the decrease of the number of DOFs is more than 1600 as well. In other words, the improvements for the HITO-MMC in iterations, objective functions are 56.5%, 11% than ITO-MMC, and the reduction of the number of DOFs is no less than 35.7%. Besides, the number of DOFs is dramatically reduced if the global refinement is replaced by the hierarchical local refinement, which can be found from the result presented in Fig. 11 and the decrement of the number of DOFs is more than 89.0% once the number of refinements is no less than 2. Therefore, the proposed HITO-MMC is very effective for solving TO problems, and with the proposed HITO-MMC, we can perform TO with relative coarse computational mesh, meanwhile the structural performance is improved.

5.2. Multiple load beam

Multiple load beam is another well-known TO benchmark, and the corresponding design domain with the dimension of 1×1, the boundary condition and volume constraint are illustrated in Fig. 12(a). The multiple beam is fixed in the left edge, loaded on right-top and right-bottom, as well as the upper bound of volume of solid material is 0.4. Moreover, the initial uniform computation mesh and basic structural components are as depicted in Fig. 12(b). The parameter tol^0_{TDF} in Eq. (22) is set to 0.1 for determining the elements to be refined.

With the aid of the HITO-MMC presented in this paper, the hierarchy computational meshes and the optimized structural topologies are illustrated in Fig. 13((a)–(e)) for intermediate iterative steps where a local refinement is conducted. Simultaneously, the final optimized result is presented in Fig. 13(f) with the same hierarchy computational mesh presented in Fig. 13(e). According to the results shown in Fig. 13, it is easy to know that the proposed HITO-MMC and mark strategy are valid for the multiple load beam example, the elements located on the boundary of structure are refined once a hierarchical local refinement is trigged. As a comparison, the optimized result obtained by ITO-MMC [34] for the current case, is depicted in Fig. 14. Compared to the result by ITO-MMC [34], the improvement in objective function is up to 15.8%, the decrease of the number of DOFs is more than 65.7% with 11.0% decrease of the number of iterations for HITO-MMC. Finally, the convergence history is presented in Fig. 15, which describes the variations of objective function and volume constraint function. From Fig. 15, it is observed that the curve of objective function is smooth expect for the iterative steps performing

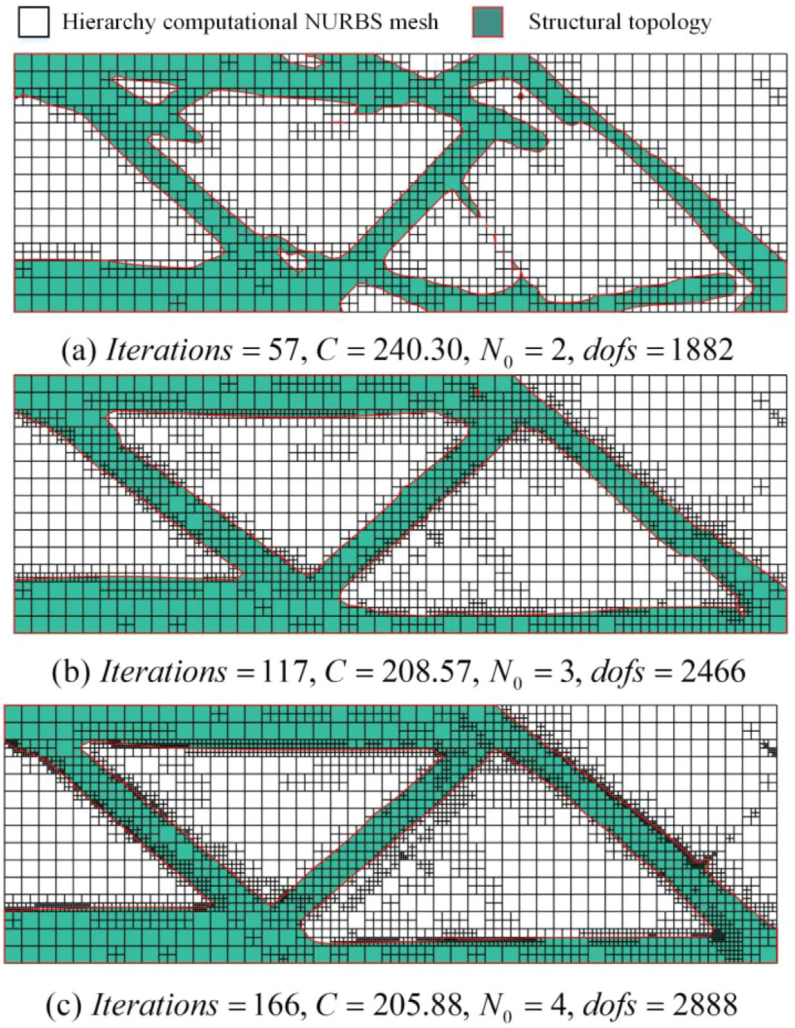

Fig. 9. The computational meshes and structural topologies for iterative steps where a hierarchical local refinement is performed, and the max hierarchical level N_0 of the hierarchy mesh is 2, 3 and 4 for (a), (b) and (c) respectively.

a local refinement and the magnitude of the mutation of objective function on steps labeled with green dotted lines is reduced with the increase of the number of max hierarchical level. The reason for this numerical phenomenon is that the ersatz material model is more accurate since the finer computational mesh is used, which results in a more accurate displacement field, and the differences in the ersatz material model of the elements close to the boundary will be reduced due to the reduced variation of the structural boundary as the TO iteration progresses.

5.3. Short beam loaded on middle of right edge

To validate the versatility of the HITO-MMC presented in this paper, short beam loaded on the middle point of right edge is examined. The top of Fig. 16 elaborates the problem setting of this benchmark, both the initial design of components and the computational mesh are illustrated in the bottom of Fig. 16. The dimension of the design domain is 2×1 and the volume of solid material is prescribed to 0.4, a vertically downward load is applied to the middle point of right edge. Besides, the mesh size of the initial computational mesh used to discretize the design domain is 28×14. To get the marked elements for the steps performing local refinement, the parameter tol^0_{TDF} in Eq. (22) takes 0.6.

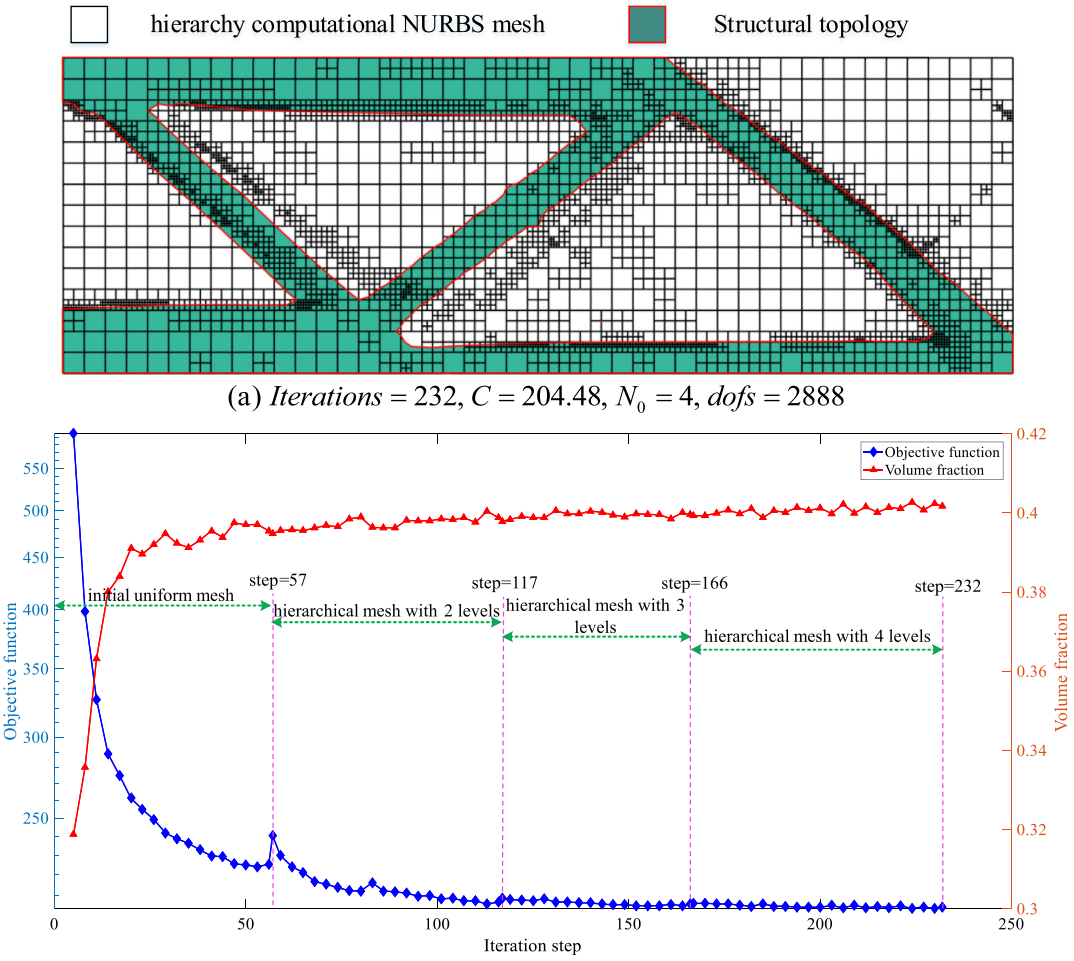

Fig. 10. The final optimized structure for half MBB is shown in (a) and the convergence history is illustrated in (b)

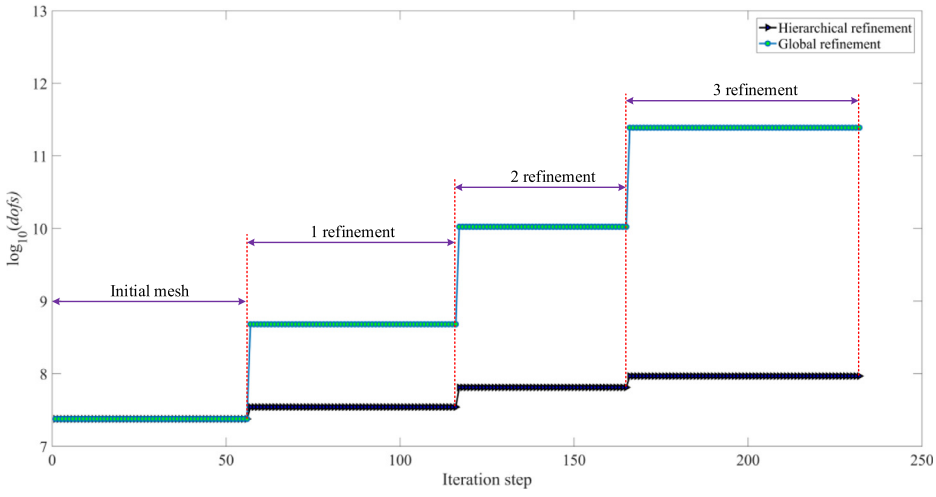

Fig. 11. A comparison of DOFs between global refinement and hierarchical local refinement of computational mesh with the same initial mesh.

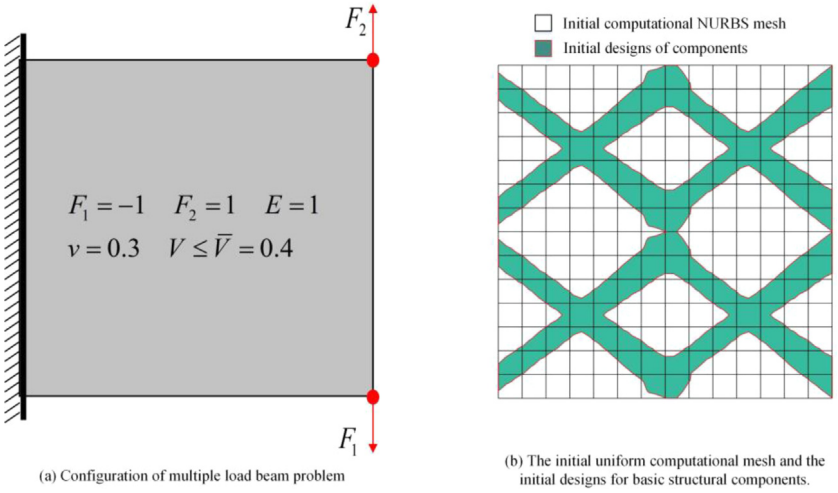

(a) Configuration of multiple load beam problem

(b) The initial uniform computational mesh and the initial designs for basic structural components.

Fig. 12. The configuration of multiple load beam is shown in (a), both initial uniform mesh with size of 14 × 14 and initial design of 8 structural components are presented in (b).

Fig. 17 depicts the computational meshes and topologies for the iterative steps where the criterion formulated as (21) is satisfied and the hierarchical local refinement is triggered. From the results shown in Fig. 17, it finds that the elements located in the neighborhood of the structural boundary are refined once the condition presented in (22) is satisfied for those elements. Therefore, the proposed mark strategy is effective for short beam as well. According to the convergence history and the final optimized structure shown in Fig. 18, it concludes that the proposed HITO-MMC is valid for short beam loaded on the middle of right edge and is versatile for all 2D minimization compliance problem. Fig. 19 presents the systematic comparisons under three different cases. From the results shown in Fig. 19, it is concluded that a globally refined NURBS mesh and the proposed HITO-MMC generate ideal results identical to the optimized structure obtained by a very dense NURBS mesh with the size of 448 × 224, and the differences in iterations are small for these three conditions, as well as the continuous refinement is helpful to improve the computational efficiency of the objective functional than fixed dense NURBS mesh. Besides, the proposed HITO-MMC outperforms the continuous global refinement in terms of the number of DOFs. Moreover, Table 1 presents a comparison between HITO-MMC and conventional MMC TO using linear Lagrange elements with three different fixed mesh sizes, which indicates that the number of DOFs is reduced by 30.1%–90.7%, the value of the objective function is improved by 10.0%–12.2%, and the number of total iterations is also reduced by 23.4%–77.8%. Hence, the proposed HITO-MMC outperforms conventional MMC TO [64].

5.4. A three dimensional cantilever problem

To extend the proposed HITO-MMC framework to three dimensional TO problems, a three dimensional cantilever is taken into account. The corresponding problem setting is illustrated in Fig. 20, where the cantilever is fixed on the surface coinciding with the green plane and subjected to a uniform linear load on the right-bottom edge, as well as the dimension of the cantilever is 1 × 1 × 0.2. As the three aforementioned benchmarks, the prescribed volume of solid material is 0.4. Besides, the parameter tol^0_{TDF} in Eq. (22) is set to 0.48 for performing the hierarchical local refinement during the process of HITO-MMC.

The initial design of components and the initial uniform mesh to discretize the design domain are presented in Fig. 21, and the size of the initial mesh is 20 × 20 × 4. Then, with the help of HITO-MMC method, the optimized topologies are obtained and shown in Fig. 22 for two intermediate steps triggering the hierarchical local refinement and the final step of the optimization. Furthermore, both the convergence history and the process of the evolution of the hierarchy computational mesh are illustrated in Fig. 23. A comparison of the number of DOFs is illustrated in Fig. 24 for both hierarchical local and global refinements, and the number of DOFs used in HITO-MMC is reduced by 90.3% than those obtained from global refinement once the number of refinements is equal to 2. Based on the

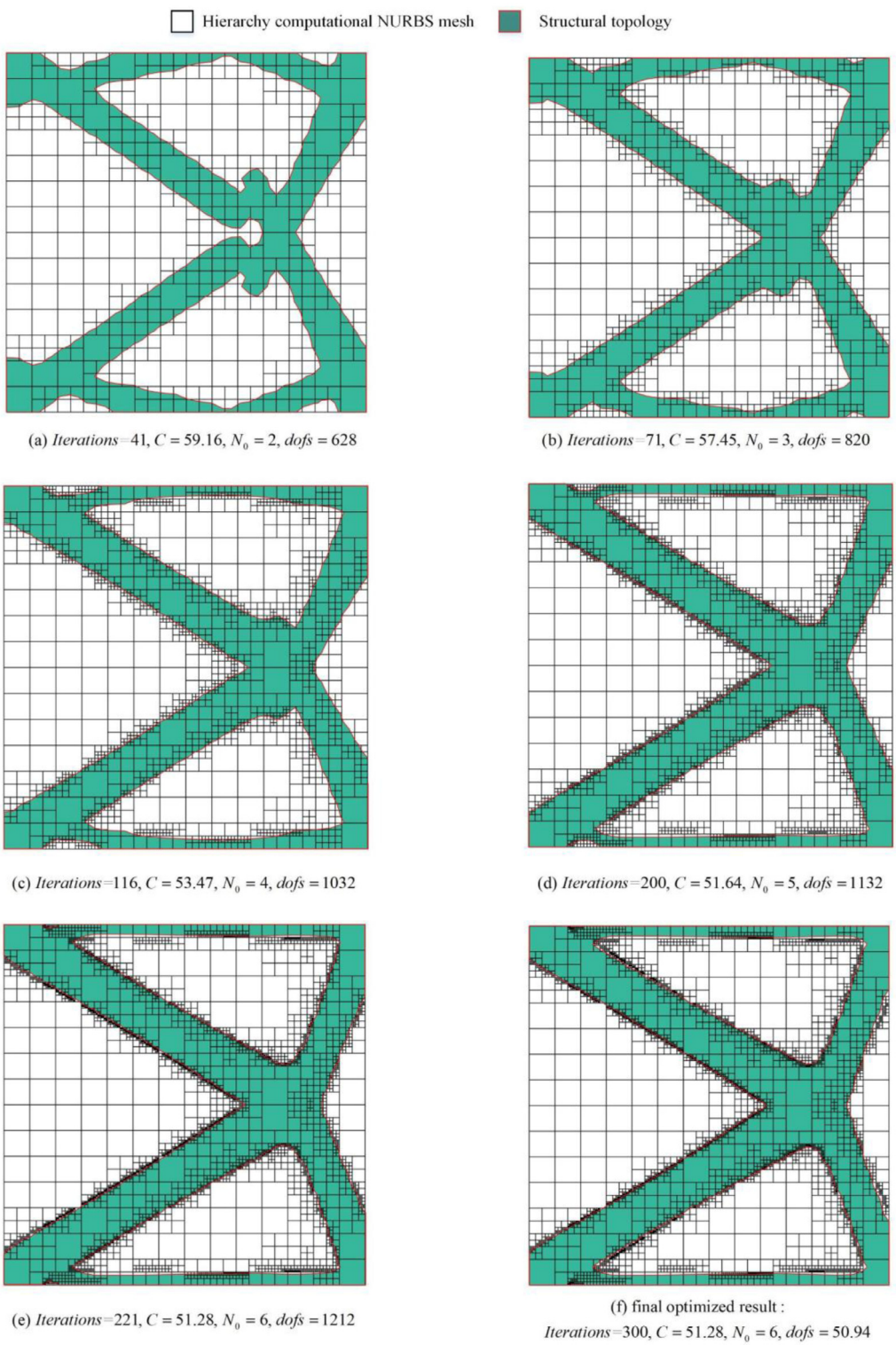

Fig. 13. The hierarchy NURBS meshes and structural topologies of intermediate iterative steps carrying out a local refinement are presented in (a)–(e), (f) is the final optimized topology and the discretized NURBS mesh for multiple load beam.

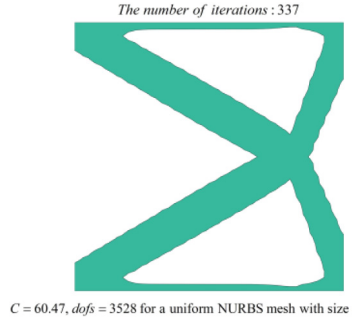

Fig. 14. The final optimized result by ITO-MMC shown in Fig. 29(a) of [34].

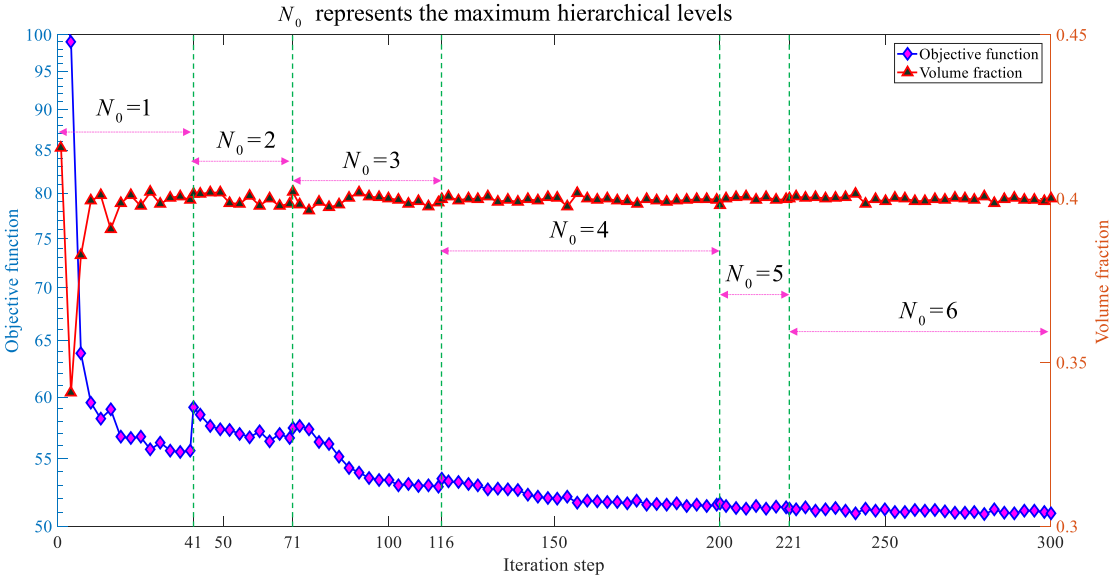

Fig. 15. The convergence history for multiple load beam optimized with the proposed HITO-MMC (a local refinement is performed on the steps labeled with green dotted lines)

results presented in Figs. 22–24, it arrives in conclusions that the proposed HITO-MMC is a promising way for solving the 3D TO problems since the number of DOFs is dramatically reduced, which results in a larger save of computational efforts, and the proposed HITO-MMC possesses the ability of optimizing the 3D structures from a relative initial coarse mesh size, as well as the hierarchical local refinement is superior to global refinement in terms of the number of DOFs.

6. Conclusions

In this work, we have developed a HITO-MMC framework based on hierarchical local refinement technique and the proposed mark strategy based on both the relative error of the objective function value and the TDF values of Gaussian points. The sensitivity analysis of HITO-MMC is derived from the relationship between global displacement vector and the local displacement vector of each level, which is computed as the sum of the hierarchical sensitivities of all levels.

According to the aforementioned numerical results, the proposed HITO-MMC is an effective tool for 2D and 3D structural TO problems, and the proposed mark strategy is capable of capturing the boundaries of the optimized structures, which leads to a more accurate ersatz material model and a more accurate displacement field on the region close to the structural boundary. Compared to ITO-MMC [27], the improvements of iterations and objective

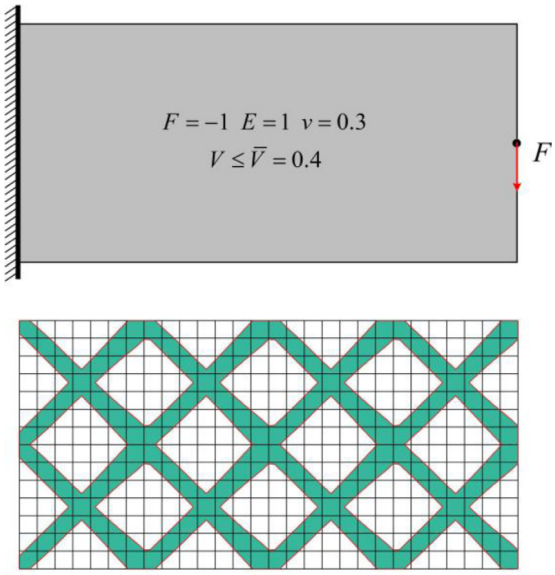

Fig. 16. The problem setting (*top*), the initial computational mesh and design of structural components (*bottom*) for short beam loaded on the middle of right edge.

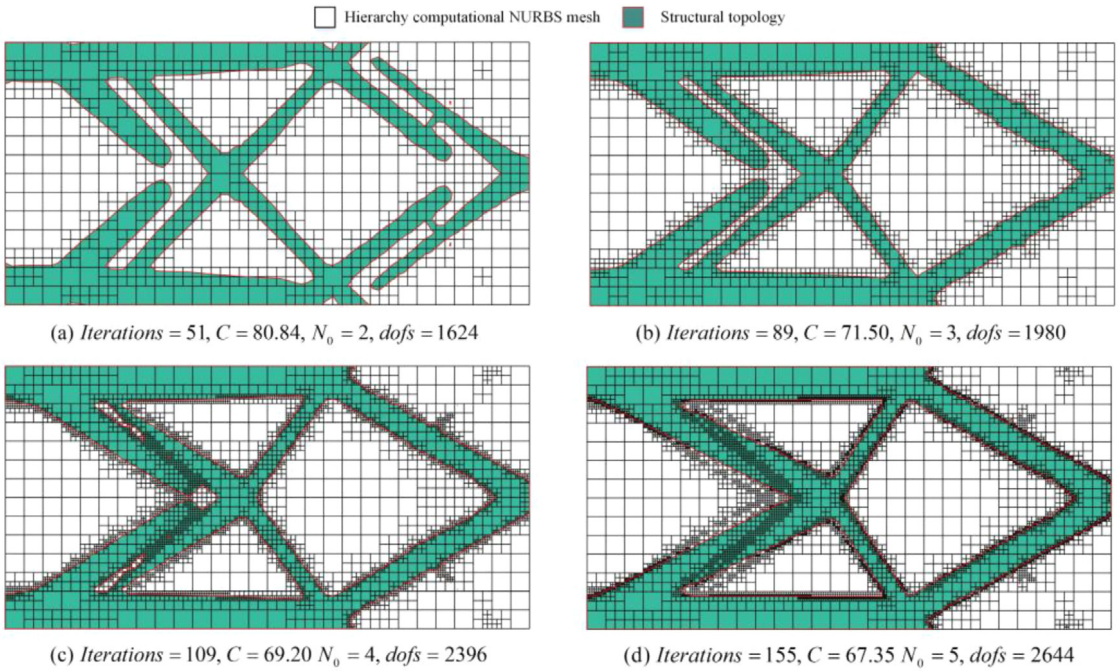

Fig. 17. The computational hierarchy meshes and structural topologies for intermediate steps with a local refinement performed.

function is 11.0%–56.5% and 11%–15.8%, meanwhile the decrement of the number of DOFs is more than 35.7% in HITO-MMC. Therefore, the proposed HITO-MMC is a more effective approach than ITO-MMC. Besides, from the results shown in Table 1, HITO-MMC outperforms the conventional MMC TO method [64] as well, since the reduction of the number of DOFs varies from 30.1% to 90.7%, the improvements of total iterations and objective function are 23.4%–77.8% and 10.0%–12.2%, respectively. The number of DOFs is reduced by 89.0% and 90.3% for

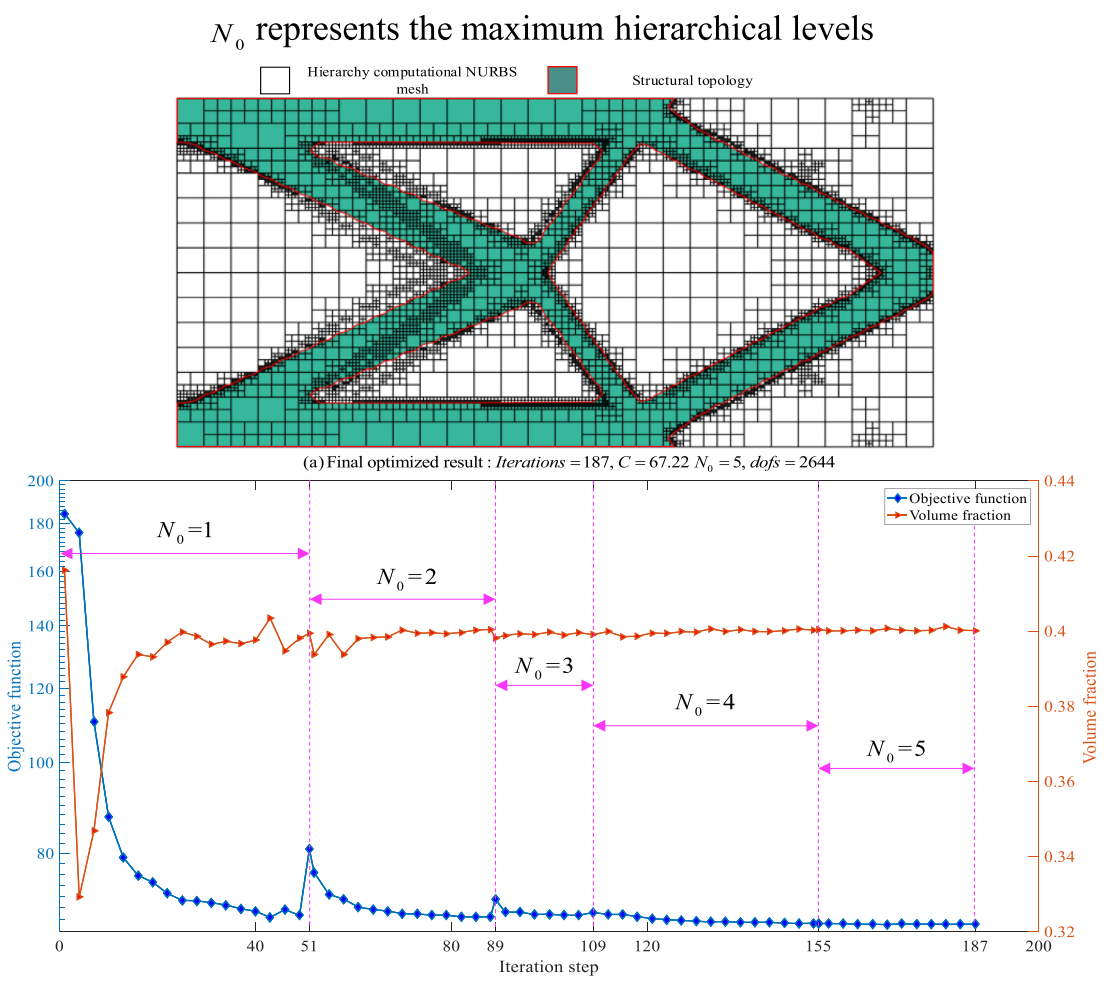

Fig. 18. The final converged structural topology and the corresponding hierarchy mesh, as well as the convergence history are presented for short beam with the HITO-MMC framework.

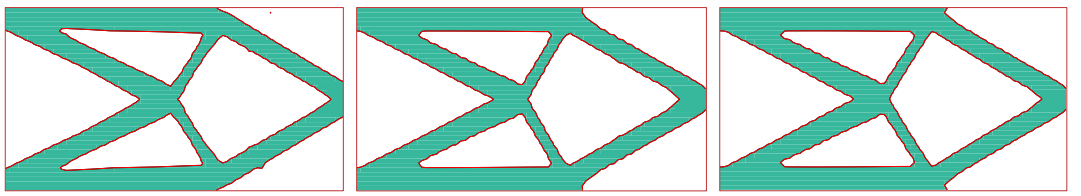

Fig. 19. Systematic comparisons between three optimized results: (a) for ITO-MMC with a 448 × 224 NURBS mesh, of which the number of DOFs is 203 400; (b) for ITO-MMC with the NURBS mesh globally refined for each refinement iterative step, of which the number of DOFs varies from 960 to 203 400; (c) for HITO-MMC with the mesh locally refined, of which the number of DOFs varying from 960 to 2644.

2D and 3D TO problems, once the global refinement is replaced by hierarchical local refinement and the number of refinements is 2. Continuous refinement outperforms the fixed NURBS mesh in generating the optimal design due to the highly computational efficiency, and hierarchical local refinement is superior to continuous uniform refinement. Hence, the proposed HITO-MMC is efficient and accurate, which has a great potential to solve large-scale TO problems.

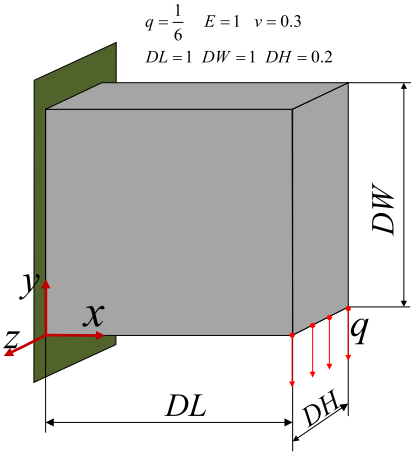

Fig. 20. The problem setting for the three dimensional cantilever problem . (For interpretation of the references to color in this figure legend, the reader is referred to the web version of this article.)

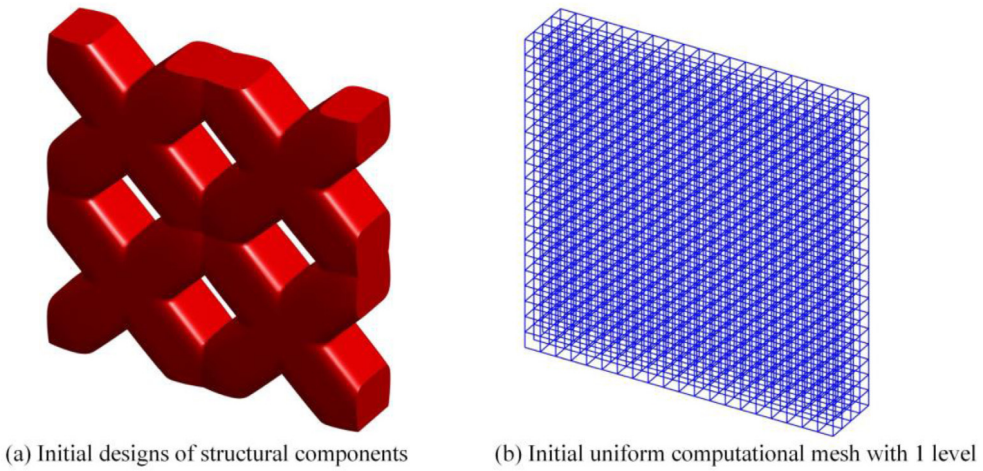

Fig. 21. The initial design of basic structural components and the uniform computational mesh used to discretize the design domain.

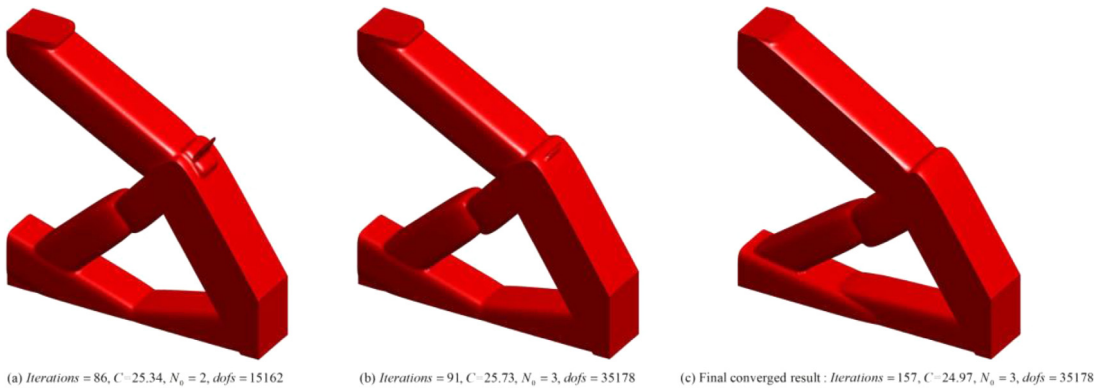

Fig. 22. The optimized structures for the steps carrying out the hierarchical local refinement and the converged step.

Table 1
A comparison between HITO-MMC and conventional MMC TO (see results in Table 1 of [34]).

Methods	HITO-MMC	Conventional MMC (60 × 30)	Improvement
DOFs (step = 1)	960		74.6%
DOFs (step = 51)	1624		57.1%
DOFs (step = 89)	1980	3782	47.7%
DOFs (step = 109)	2396		36.7%
DOFs (step = 155)	2644		30.1%
Final optimized C	67.22	76.52	12.2%
Total iterations	187	464	59.7%
Methods	HITO-MMC	Conventional MMC (80 × 40)	Improvement
DOFs (step = 1)	960		85.6%
DOFs (step = 51)	1624		75.6%
DOFs (step = 89)	1980	6642	70.2%
DOFs (step = 109)	2396		63.9%
DOFs (step = 155)	2644		60.2%
Final optimized C	67.22	74.68	10.0%
Total iterations	187	244	23.4%
Methods	HITO-MMC	Conventional MMC (100 × 50)	Improvement
DOFs (step = 1)	960		90.7%
DOFs (step = 51)	1624		84.2%
DOFs (step = 89)	1980	10 302	80.8%
DOFs (step = 109)	2396		76.7%
DOFs (step = 155)	2644		74.3%
Final optimized C	67.22	74.66	10.0%
Total iterations	187	841	77.8%

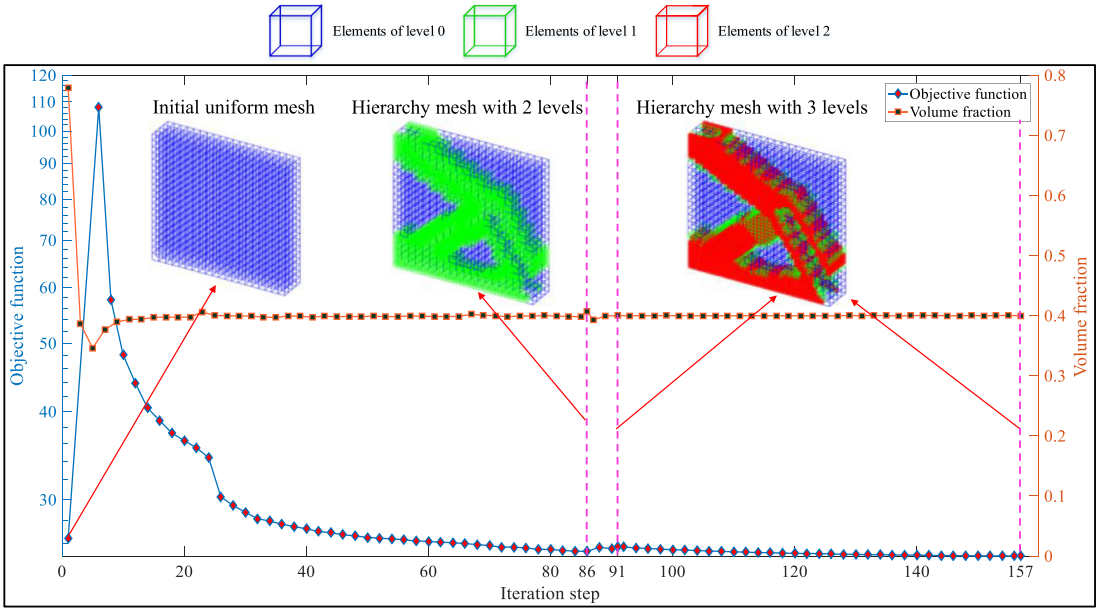

Fig. 23. The convergence history for the 3D cantilever TO problem and the evolution of the hierarchy computational mesh for the discretization of the design domain.

Since the coarsening is not incorporated into current method, hierarchical coarsening algorithm should be taken into consideration for the benefit of making the HITO-MMC fully dynamic and reducing the number of DOFs

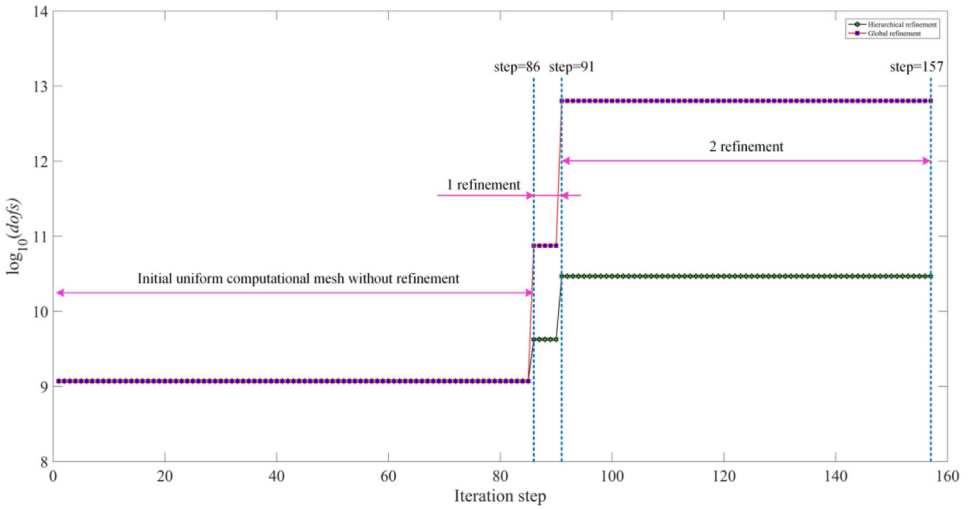

Fig. 24. An illustration for the comparison of the number of DOFs between hierarchical local refinement and global refinement.

further. Due to the local refinement ability of HITO-MMC, the HITO-MMC can applied to the TO problems with geometric singularity and can extend to optimize the piezoresistive pressure sensor [68] considering a stress constraint more effectively. Besides, the GPU parallel computing [69] can be added into such a HITO-MMC model to further improve the computational efficiency. These objectives will be carried out in our future research works.

Acknowledgments

This work has been supported by National Natural Science Foundation of China (51675197, 51705158), the Fundamental Research Funds for the Central Universities (2018MS45), and Open Funds of National Engineering Research Center of Near-Net-Shape Forming for Metallic Materials (2018005). These supports are gratefully acknowledged.

Appendix. Sensitivity analysis of HITO-MMC

The derivative of compliance C presented in Eq. (39) with respect to an arbitrary geometric design variable a_j with $a_j \in \boldsymbol{D}$ is acquired by differentiating both sides of the objective function of HITO-MMC model, which is formulated as:

$$\frac{\partial C}{\partial a_j} = \sum_{l=0}^{N_0-1}\sum_{e=1}^{N_e^l} \frac{\partial((\boldsymbol{u}_e^l)^{\mathrm{T}}\overline{\boldsymbol{K}}_e^l\boldsymbol{u}_e^l)}{\partial a_j} = \sum_{l=0}^{N_0-1}\sum_{e=1}^{N_e^l}\left(\frac{\partial(\boldsymbol{u}_e^l)^{\mathrm{T}}}{\partial a_j}\overline{\boldsymbol{K}}_e^l\boldsymbol{u}_e^l + (\boldsymbol{u}_e^l)^{\mathrm{T}}\frac{\partial\overline{\boldsymbol{K}}_e^l}{\partial a_j}\boldsymbol{u}_e^l + (\boldsymbol{u}_e^l)^{\mathrm{T}}\overline{\boldsymbol{K}}_e^l\frac{\partial\boldsymbol{u}_e^l}{\partial a_j}\right). \tag{40}$$

Based on the adjoint sensitivity analysis and the chain rule as well as the relationship presented in Eq. (35), the formula shown above can be rearranged as a sum of the hierarchical sensitivities of all hierarchical levels:

$$\begin{aligned}&\frac{\partial C}{\partial a_j} = \frac{\partial C}{\partial a_j} = \sum_{l=0}^{N_0-1}\frac{\partial C^l}{\partial a_j}\\ &\text{with } \frac{\partial C^l}{\partial a_j} = \sum_{e=1}^{N_e^l}\left\{(\boldsymbol{u}_e^l)\cdot q\cdot\frac{1}{n_{gp}}\left(\sum_{i=1}^{n_{gp}}H_\varepsilon(\varphi_i)^{q-1}\frac{\partial H_\varepsilon(\varphi_i)}{\partial a_j}\right)_e\cdot\boldsymbol{K}_e^l\boldsymbol{u}_e^l\right\}(q=2).\end{aligned} \tag{41}$$

Moreover, the sensitivity of the volume constraint function is written as:

$$\frac{\partial V}{\partial a_j} = \sum_{l=0}^{N_0-1} \frac{\partial V^l}{\partial a_j}$$
$$\text{with } \frac{\partial V^l}{\partial a_j} = \frac{1}{n_{gp}} \sum_{e=1}^{N_e^l} \left(\sum_{i=1}^{n_{gp}} \frac{\partial H(\varphi_i)}{\partial a_j} \right)_e V_e^l. \tag{42}$$

References

[1] M.P. Bendsoe, N. Kikuchi, Generating optimal topologies in structural design using a homogenization method, Comput. Methods Appl. Mech. Engrg. 71 (2) (1988) 197–224.
[2] M.P. Bendsøe, Optimal shape design as a material distribution problem, Struct. Optim. 1 (4) (1989) 193–202.
[3] Y.M. Xie, G.P. Steven, A simple evolutionary procedure for structural optimization, Comput. Struct. 49 (5) (1993) 885–896.
[4] G. Allaire, F. Jouve, A.M. Toader, Structural optimization using sensitivity analysis and a level-set method, J. Comput. Phys. 194 (1) (2004) 363–393.
[5] Y. Mei, X. Wang, A level set method for structural topology optimization and its applications, Comput. Methods Appl. Mech. Engrg. 35 (7) (2004) 415–441.
[6] H. Li, Z. Luo, L. Gao, Q. Qin, Topology optimization for concurrent design of structures with multi-patch microstructures by level sets, Comput. Methods Appl. Mech. Engrg. 331 (2018) 536–561.
[7] J. Liu, Y. Ma, A new multi-material level set topology optimization method with the length scale control capability, Comput. Methods Appl. Mech. Engrg. 329 (2018) 444–463.
[8] X. Guo, Doing topology optimization explicitly and geometrically—a new moving morphable components based framework, Front. Appl. Mech. 81 (8) (2014) 081009.
[9] W. Zhang, D. Li, J. Zhou, Z. Du, B. Li, X. Guo, A Moving Morphable Void (MMV)-based explicit approach for topology optimization considering stress constraints, Comput. Methods Appl. Mech. Engrg. (2018).
[10] W. Hou, Y. Gai, X. Zhu, X. Wang, C. Zhao, L. Xu, K. Jiang, P. Hu, Explicit isogeometric topology optimization using moving morphable components, Comput. Methods Appl. Mech. Engrg. 326 (2017) 694–712.
[11] W. Zhang, J. Song, J. Zhou, Z. Du, Y. Zhu, Z. Sun, X. Guo, Topology optimization with multiple materials via Moving Morphable Component (MMC) method, Internat. J. Numer. Methods Engrg. 113 (11) (2017) 1653–1675.
[12] T. Liu, B. Li, S. Wang, L. Gao, Eigenvalue topology optimization of structures using a parameterized level set method, Struct. Multidiscip. Optim. 50 (4) (2014) 573–591.
[13] T. Liu, S. Wang, B. Li, L. Gao, A level-set-based topology and shape optimization method for continuum structure under geometric constraints, Struct. Multidiscip. Optim. 50 (2) (2014) 253–273.
[14] T. Zegard, G.H. Paulino, Bridging topology optimization and additive manufacturing, Struct. Multidiscip. Optim. 53 (1) (2016) 175–192.
[15] Y. Wang, S. Arabnejad, M. Tanzer, D. Pasini, Hip implant design with three-dimensional porous architecture of optimized graded density, J. Mech. Des. 140 (11) (2018) 111406–111406–111413.
[16] C.J. Brampton, H.A. Kim, J.L. Cunningham, Level set topology optimisation of aircraft wing considering aerostructural interaction, Arch. Comput. Method Eng. (2012).
[17] Q. Xia, T. Shi, S. Liu, M.Y. Wang, Shape and topology optimization for tailoring stress in a local region to enhance performance of piezoresistive sensors, Comput. Struct. 114 (2013) 98–105.
[18] N. Aage, E. Andreassen, B.S. Lazarov, O. Sigmund, Giga-voxel computational morphogenesis for structural design, Nature 550 (7674) (2017) 84–86.
[19] J. Dirker, J.P. Meyer, Topology optimization for an internal heat-conduction cooling scheme in a square domain for high heat flux applications, J. Heat Trans.-T ASME 135 (11) (2013) 111010.
[20] M. Langelaar, Topology optimization of 3D self-supporting structures for additive manufacturing, Addit. Manuf. 12 (2016) 60–70.
[21] O. Sigmund, J. Petersson, Numerical instabilities in topology optimization: A survey on procedures dealing with checkerboards, mesh-dependencies and local minima, Struct. Optim. 16 (1) (1998) 68–75.
[22] Y. Wang, Z. Wang, Z. Xia, L.H. Poh, Structural design optimization using isogeometric analysis: A comprehensive review, CMES-Comput. Model. Eng. Sci. 117 (3) (2018) 455–507.
[23] T.J.R. Hughes, J.A. Cottrell, Y. Bazilevs, Isogeometric analysis: CAD, finite elements, NURBS, exact geometry and mesh refinement, Comput. Methods Appl. Mech. Engrg. 194 (39–41) (2005) 4135–4195.
[24] X. Qian, Topology optimization in B-spline space, Comput. Methods Appl. Mech. Engrg. 265 (3) (2013) 15–35.
[25] X. Qian, Full analytical sensitivities in NURBS based isogeometric shape optimization, Comput. Methods Appl. Mech. Engrg. 199 (29) (2010) 2059–2071.
[26] H. Liu, D. Yang, P. Hao, X. Zhu, Isogeometric analysis based topology optimization design with global stress constraint, Comput. Methods Appl. Mech. Engrg. 342 (2018) 625–652.
[27] L. Dedè, M.J. Borden, T.J.R. Hughes, Isogeometric analysis for topology optimization with a phase field model, Arch. Comput. Method Eng. 19 (3) (2012) 427–465.
[28] B. Hassani, M. Khanzadi, S.M. Tavakkoli, An isogeometrical approach to structural topology optimization by optimality criteria, Struct. Multidiscip. Optim. 45 (2) (2012) 223–233.

[29] Q.X. Lieu, J. Lee, A multi-resolution approach for multi-material topology optimization based on isogeometric analysis, Comput. Methods Appl. Mech. Engrg. 323 (2017) 272–302.
[30] Y. Wang, D.J. Benson, Isogeometric analysis for parameterized LSM-based structural topology optimization, Comput. Mech. 57 (1) (2016) 19–35.
[31] Y. Wang, D.J. Benson, Geometrically constrained isogeometric parameterized level-set based topology optimization via trimmed elements, Front. Mech. Eng. 11 (4) (2016) 1–16.
[32] Y. Wang, H. Xu, D. Pasini, Multiscale isogeometric topology optimization for lattice materials, Comput. Methods Appl. Mech. Engrg. 316 (2016) 568–585.
[33] C. Liu, Y. Zhu, Z. Sun, D. Li, Z. Du, W. Zhang, X. Guo, An efficient moving morphable component (MMC)-based approach for multi-resolution topology optimization, Struct. Multidiscip. Optim. 58 (6) (2018) 2455–2479.
[34] X. Xie, S. Wang, M. Xu, Y. Wang, A new isogeometric topology optimization using moving morphable components based on r-functions and collocation schemes, Comput. Methods Appl. Mech. Engrg. 339 (2018) 61–90.
[35] A. Nana, J.-C. Cuillière, V. Francois, Towards adaptive topology optimization, Adv. Eng. Softw. 100 (2016) 290–307.
[36] M.A.S. de Troya, D.A. Tortorelli, Adaptive mesh refinement in stress-constrained topology optimization, Struct. Multidiscip. Optim. 58 (6) (2018) 2369–2386.
[37] A.B. Lambe, A. Czekanski, Topology optimization using a continuous density field and adaptive mesh refinement, Internat. J. Numer. Methods Engrg. 113 (3) (2018) 357–373.
[38] Y. Bazilevs, V.M. Calo, J.A. Cottrell, J.A. Evans, T.J.R. Hughes, S. Lipton, M.A. Scott, T.W. Sederberg, Isogeometric analysis using T-splines, Comput. Methods Appl. Mech. Engrg. 199 (5–8) (2010) 229–263.
[39] M.A. Scott, M.J. Borden, C.V. Verhoosel, T.W. Sederberg, T.J. Hughes, Isogeometric finite element data structures based on Bézier extraction of T-splines, Internat. J. Numer. Methods Engrg. 88 (2) (2011) 126–156.
[40] M.A. Scott, X. Li, T.W. Sederberg, T.J. Hughes, Local refinement of analysis-suitable T-splines, Comput. Methods Appl. Mech. Engrg. 213 (2012) 206–222.
[41] K.A. Johannessen, T. Kvamsdal, T. Dokken, Isogeometric analysis using LR B-splines, Comput. Methods Appl. Mech. Engrg. 269 (2014) 471–514.
[42] R. Kraft, Adaptive and linearly independent multilevel B-splines, SFB 404, Geschäftsstelle, 1997.
[43] A.-V. Vuong, C. Giannelli, B. Jüttler, B. Simeon, A hierarchical approach to adaptive local refinement in isogeometric analysis, Comput. Methods Appl. Mech. Engrg. 200 (49–52) (2011) 3554–3567.
[44] C. Giannelli, B. Jüttler, H. Speleers, Strongly stable bases for adaptively refined multilevel spline spaces, Adv. Comput. Math. 40 (2) (2014) 459–490.
[45] D. Schillinger, L. Dede, M.A. Scott, J.A. Evans, M.J. Borden, E. Rank, T.J. Hughes, An isogeometric design-through-analysis methodology based on adaptive hierarchical refinement of nurbs, immersed boundary methods, and T-spline CAD surfaces, Comput. Methods Appl. Mech. Engrg. 249 (2012) 116–150.
[46] T. Kanduč, C. Giannelli, F. Pelosi, H. Speleers, Adaptive isogeometric analysis with hierarchical box splines, Comput. Methods Appl. Mech. Engrg. 316 (2017) 817–838.
[47] P. Hennig, S. Müller, M. Kästner, Bézier extraction and adaptive refinement of truncated hierarchical NURBS, Comput. Methods Appl. Mech. Engrg. 305 (2016) 316–339.
[48] P. Bornemann, F. Cirak, A subdivision-based implementation of the hierarchical b-spline finite element method, Comput. Methods Appl. Mech. Engrg. 253 (2013) 584–598.
[49] E.M. Garau, R. Vázquez, Algorithms for the implementation of adaptive isogeometric methods using hierarchical B-splines, Appl. Numer. Math. 123 (2018) 58–87.
[50] G. Kiss, C. Giannelli, B. Jüttler, Algorithms and data structures for truncated hierarchical B–splines, in: International Conference on Mathematical Methods for Curves and Surfaces, Springer, 2012, pp. 304–323.
[51] C. Giannelli, B. JüTtler, H. Speleers, THB-splines: The truncated basis for hierarchical splines, Comput. Aided Geom. D 29 (7) (2012) 485–498.
[52] S. Wang, E. de Sturler, G.H. Paulino, Dynamic adaptive mesh refinement for topology optimization, arXiv preprint arXiv:1009.4975, 2010.
[53] K. Maute, E. Ramm, Adaptive topology optimization, Struct. Optim. 10 (2) (1995) 100–112.
[54] Z. Liao, Y. Zhang, Y. Wang, W. Li, A triple acceleration method for topology optimization, Struct. Multidiscip. Optim. (2019) 1–18.
[55] A.V. Vuong, C. Giannelli, B. Jüttler, B. Simeon, A hierarchical approach to adaptive local refinement in isogeometric analysis, Comput. Methods Appl. Mech. Engrg. 200 (49) (2012) 3554–3567.
[56] J.A. Cottrell, T.J.R. Hughes, Y. Bazilevs, Isogeometric Analysis: Toward Integration of CAD and FEA, Vol. 141, Wiley & Sons, 2015, pp. 299–325, (5).
[57] L. Piegl, W. Tiller, The NURBS Book, Springer Berlin Heidelberg, 1997.
[58] B. Marussig, T.J.R. Hughes, A review of trimming in isogeometric analysis: Challenges, data exchange and simulation aspects, Arch. Comput. Method Eng. (8) (2017) 1–69.
[59] C.K. Chui, An Introduction to Wavelets, Elsevier, 2016.
[60] J. Warren, H. Weimer, Subdivision Methods for Geometric Design: A Constructive Approach, Elsevier, 2001.
[61] D. Zorin, Subdivision for modeling and animation, SIGGRAPH2000 course notes, 2000.
[62] J. Peters, U. Reif, Subdivision Surfaces, Springer, 2008.
[63] M. Sabin, Analysis and Designb of Univariate Subdivision Schemes, Springer, 2010.
[64] W. Zhang, J. Yuan, J. Zhang, X. Guo, A new topology optimization approach based on Moving Morphable Components (MMC) and the ersatz material model, Struct. Multidiscip. Optim. 53 (6) (2016) 1243–1260.

[65] X. Guo, W. Zhang, J. Zhang, J. Yuan, Explicit structural topology optimization based on moving morphable components (MMC) with curved skeletons, Comput. Methods Appl. Mech. Engrg. 310 (2016) 711–748.
[66] D. Schillinger, J.A. Evans, A. Reali, M.A. Scott, T.J. Hughes, Isogeometric collocation: Cost comparison with Galerkin methods and extension to adaptive hierarchical NURBS discretizations, Comput. Methods Appl. Mech. Engrg. 267 (2013) 170–232.
[67] K. Svanberg, The method of moving asymptotes—a new method for structural optimization, Internat. J. Numer. Methods Engrg. 24 (2) (1987) 359–373.
[68] A.V. Tran, X. Zhang, B. Zhu, The development of a new piezoresistive pressure sensor for low pressures, IEEE Trans. Ind. Electron. 65 (8) (2017) 6487–6496.
[69] Z. Xia, Y. Wang, Q. Wang, C. Mei, GPU parallel strategy for parameterized LSM-based topology optimization using isogeometric analysis, Struct. Multidiscip. Optim. 56 (2) (2017) 1–22.